Volume 16
Number 18
14 May 2025
Pages 7593–8138

Chemical Science

rsc.li/chemical-science

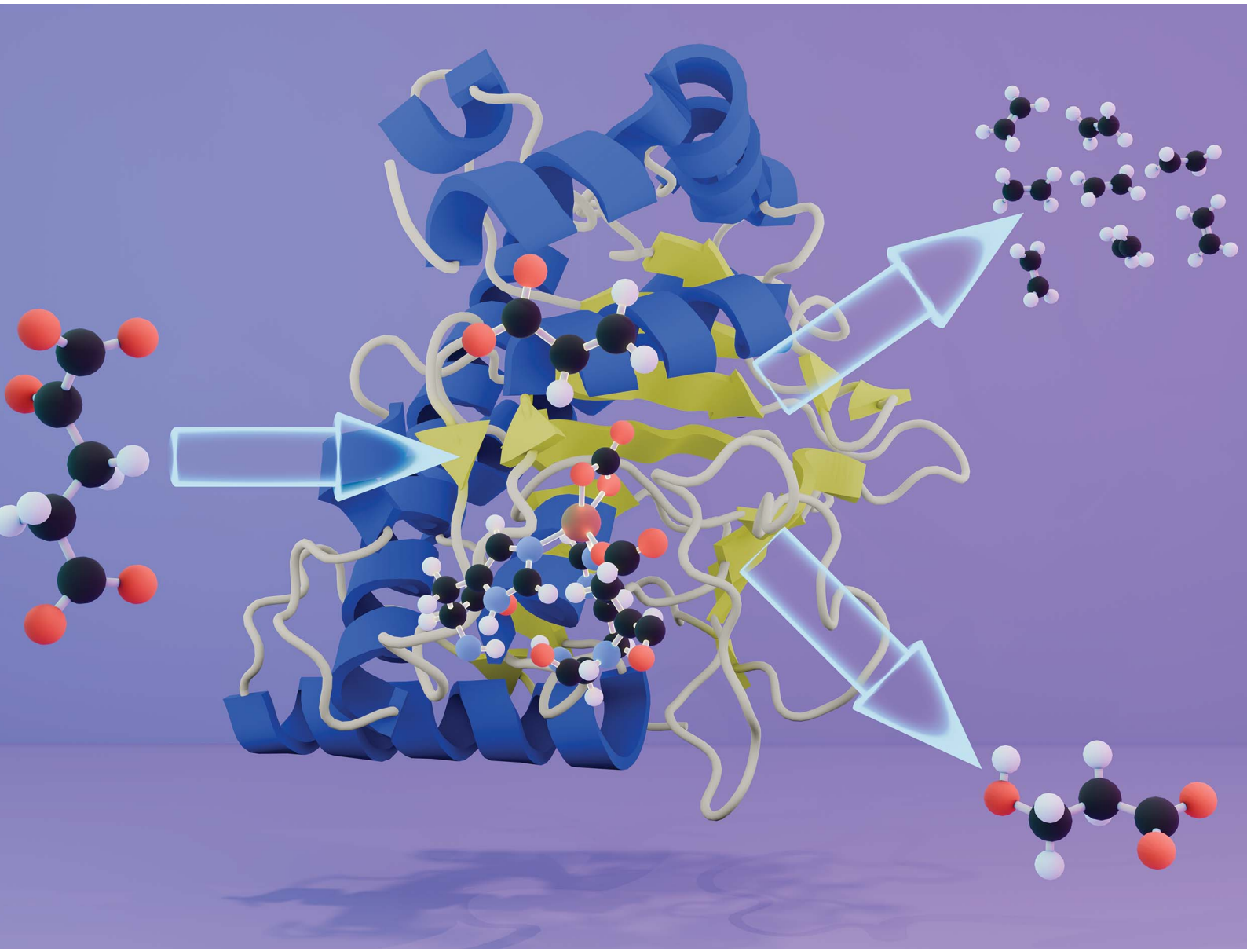

ISSN 2041-6539

ROYAL SOCIETY OF CHEMISTRY

EDGE ARTICLE

Christo Z. Christov *et al.*

Revealing the nature of the second branch point in the catalytic mechanism of the Fe(II)/2OG-dependent ethylene forming enzyme

15 YEARS ANNIVERSARY

Chemical Science

ROYAL SOCIETY OF CHEMISTRY

EDGE ARTICLE

View Article Online
View Journal | View Issue

Cite this: *Chem. Sci.*, 2025, **16**, 7667

All publication charges for this article have been paid for by the Royal Society of Chemistry

Revealing the nature of the second branch point in the catalytic mechanism of the Fe(II)/2OG-dependent ethylene forming enzyme†

Simahudeen Bathir Jaber Sathik Rifayee, Midhun George Thomas and Christo Z. Christov *

Ethylene-forming enzyme (EFE) has economic importance due to its ability to catalyze the formation of ethylene and 3-hydroxypropionate (3HP). Understanding the catalytic mechanism of EFE is essential for optimizing the biological production of these important industrial chemicals. In this study, we implemented molecular dynamics (MD) and quantum mechanics/molecular mechanics (QM/MM) to elucidate the pathways leading to ethylene and 3HP formation. Our results suggest that ethylene formation occurs from the propion-3-yl radical intermediate rather than the (2-carboxyethyl)carbonato-Fe(II) (**EFIV**) intermediate, which conclusively acts as a precursor for 3HP formation. The results also explain the role of the hydrophobic environment surrounding the 2OG binding site in stabilizing the propion-3-yl radical, which defines their conversion to either ethylene or 3HP. Our simulations on the A198L EFE variant, which produces more 3HP than wild-type (WT) EFE based on experimental observations, predict that the formation of the **EFIV** intermediate was more favored than WT. Also, MD simulations on the **EFIV** intermediate in both WT and A198L EFE predicted that the water molecules approach the Fe center, which suggests the role of water molecules in the breakdown of the **EFIV** intermediate. QM/MM simulations on the **EFIV** intermediate of WT and A198L EFE predicted that the Fe-bound water molecule could provide a proton for the 3HP formation from **EFIV**. The study underscores the critical influence of the enzyme's hydrophobic environment and second coordination sphere residues in determining product distribution between ethylene and 3HP. These mechanistic insights lay a foundation for targeted enzyme engineering, aiming to improve the selectivity and catalytic efficiency of EFE in biological ethylene and 3HP production.

Received 11th December 2024
Accepted 13th March 2025

DOI: 10.1039/d4sc08378d

rsc.li/chemical-science

1. Introduction

Ethylene is an important organic compound due to its abundant use as an industrial chemical and a precursor in synthesizing several other organic molecules.[1,2] Ethylene biosynthesis has gained focus recently due to the depletion of ethylene sources such as fossil fuels and the increase in global energy demand.[3] The primary source of ethylene production involves burning carbon feedstocks from the fossil fuel industry.[4] Biological sources have gained traction recently for a greener way to synthesize ethylene.[5] Ethylene is produced through different biological processes by plants and microbes such as bacteria and fungi.[5] It is made from various starting materials due to the action of certain enzymes. For example, in plants, ethylene is formed from methionine through oxidation of 1-aminocyclopropane-1-carboxylic acid (ACC) by an ACC oxidase enzyme.[6–9] However, the toxic byproduct of this process (cyanide) has limited its use in large-scale ethylene production.[10] Some microorganisms produce ethylene in trace quantities, which is not appealing to be considered for widespread exploration.[11,12] However, in the case of bacteria such as *Pseudomonas syringae* and *Ralstonia solanacearum* and fungus *Penicillium digitatum*, ethylene is produced in large amounts through the catalysis of Ethylene-Forming Enzyme (EFE).[13–16]

EFE is an iron(II)(Fe(II)) and 2-oxoglutarate (2OG)-dependent (Fe(II)/2OG) oxygenase containing a characteristic double sheet beta-helix (DSBH) fold with distinct reactivities (Fig. 1).[17–20] The canonical reactions catalyzed by Fe(II)/2OG-dependent oxygenases involve hydroxylation, epimerization, desaturation, cyclization, and ring-expansion reactions of the substrate through a reactive ferryl intermediate.[21,22]

EFE conforms to these functionalities only in its minor reaction involving the two-electron oxidative decarboxylation of co-substrate 2-OG to form succinate and Fe(IV)=O (ferryl) that hydroxylates the native substrate L-arginine (L-Arg) at C5 carbon (**RO**), which further undergoes oxidative fragmentation to form

Department of Chemistry, Michigan Technological University, Houghton, MI-49931, USA. E-mail: christov@mtu.edu

† Electronic supplementary information (ESI) available: Coordinates of the optimized structures and the absolute energies obtained during QM/MM simulations and additional images. See DOI: https://doi.org/10.1039/d4sc08378d

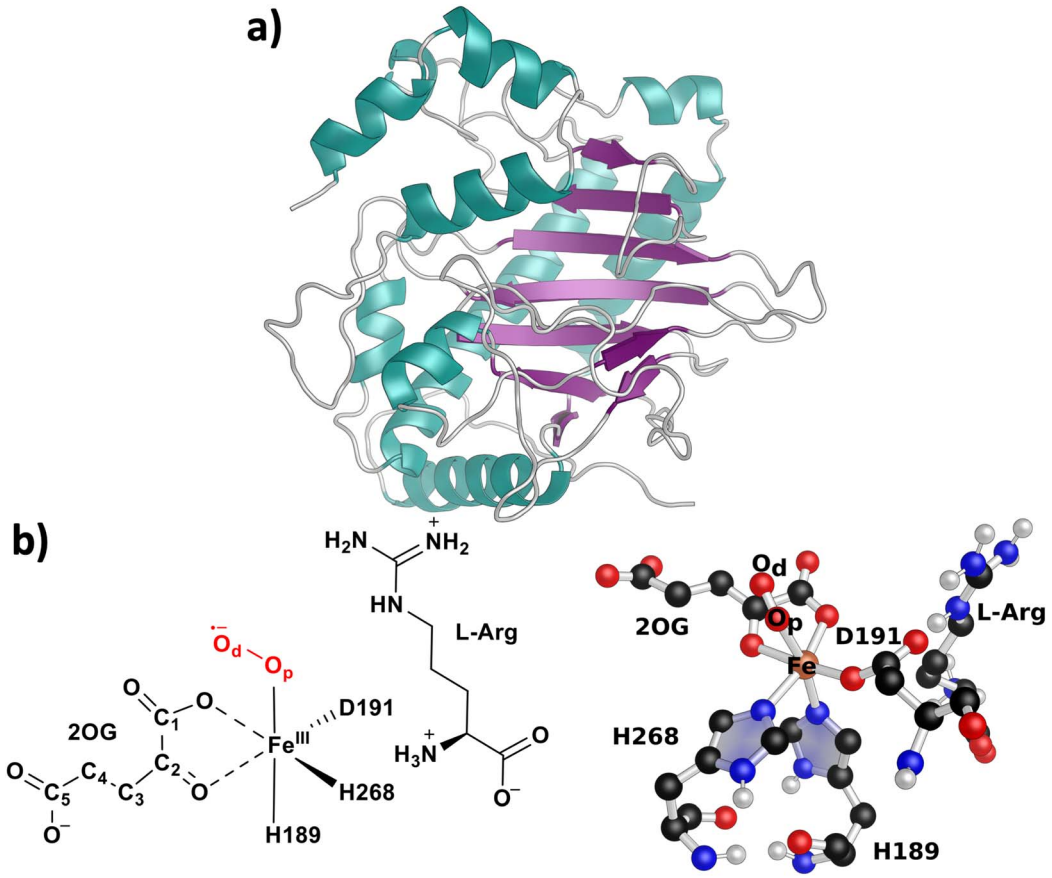

Fig. 1 (a) Overall fold of EFE (PDB ID: 5v2y). Violet-colored regions represent the β-sheets, and teal-colored regions represent the α-helices. (b) The skeletal and 3D representation of the computationally modeled EFE active site depicting Fe(III) bonded with the facial triad, 2OG, superoxide, and substrate L-Arg. Non-polar hydrogens are hidden for clarity.

pyrroline 5-carboxylate (P5C) and guanidine.[23] The major pathway of EFE, however, involves the atypical breakdown of prime substrate 2OG through four-electron oxidation to form ethylene (**EF**) (Fig. 2a). Although L-Arg is not involved in the EF pathway, it has been reported that the binding of L-Arg is essential for the reactions catalyzed by EFE.[17] Also, very recently, a third reaction catalyzed by EFE was experimentally determined by Bollinger *et al.*, which involved the breakdown of 2OG to 3-hydroxypropionate (3HP),[24,25] an important feedstock used to synthesize a wide range of chemicals, including acrylic acid, malonic acid, acrylamide, acrylonitrile, and poly-3HP based polymers.[26] The reaction mechanism of EFE initiates through the binding of dioxygen (O_2) to Fe, which was proposed to give an Fe(III)–$OO^{\bullet -}$ intermediate (Fig. 1b);[27] however, it is yet to be experimentally determined. The branch point between the EF:RO pathway was postulated to be at the O_2 activation step of the mechanism where the attack of distal oxygen (O_d) of Fe(III)–$OO^{\bullet -}$ on the C2 carbon of 2OG leads to the formation of peroxysuccinate (**RO-I**) through C1 decarboxylation which subsequently proceeds to the RO pathway while the succinyl-peroxocarbonato-Fe(II) (**EFI**) formation through O_2 insertion between C1–C2 proceeds to the EF pathway (Fig. 2b).[24,28,29] The **RO-I** intermediate undergoes cleavage of the O_p–O_d bond to form ferryl and succinate (**RO-II**). The ferryl intermediate abstracts hydrogen from the C5-carbon of L-Arg to form the hydroxo-Fe(III) complex and C5-carbon radical (**RO-III**). The subsequent rebound of the hydroxo group to the C5-carbon results in C-5 hydroxylated L-Arg (**RO-IV**).[23] In contrast, the **EFI** intermediate was computationally proposed to undergo O_p–O_d bond homolytic cleavage to form a succinyl radical and C1-derived carbonato-Fe(III) (**EFII**) intermediate.[20,24,29,30] The succinyl radical was proposed to initiate radical decarboxylation to give a propion-3-yl radical (**EFIII**). The radical coupling of C3 of the propion-3-yl radical to carbonato-Fe(III) leads to the formation of the (2-carboxyethyl)carbonato-Fe(II) (**EFIV**) intermediate. The second branch point that leads to ethylene and 3HP production is along the EF pathway; however, the intermediate state at which this branching occurs is still under discussion. Bollinger *et al.* proposed that the branching occurs at the **EFIV** state.[24,28] The **EFIV** intermediate was proposed to undergo a Grob-like polar concerted fragmentation to give CO_2, ethylene, and carbonate or partial fragmentation to give 3HP and C2-derived CO_2.[24,28] However, the suggested pathway was based on isotope labeling and product analysis with different 2OG modifications, considering the steric effects and stringent requirements for the *anti*-periplanar disposition of the electrofuge (carboxylate of **EFIV**) and nucleofuge (carbonate of **EFIV**).[24,28] In addition to the steric effects, there would be electronic factors upon which the

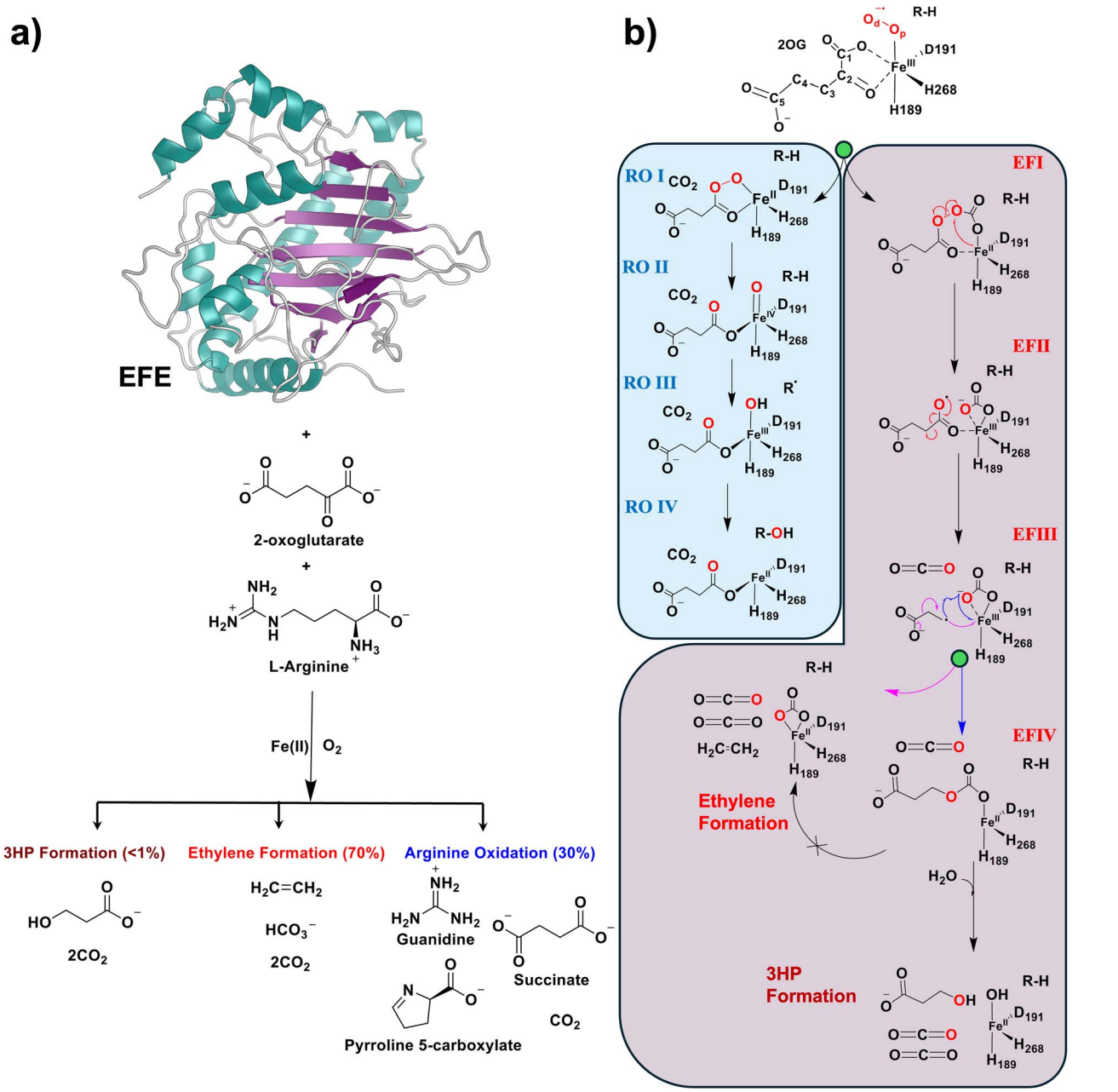

Fig. 2 (a) Reactions catalyzed by the ethylene-forming enzyme (EFE). (b) Mechanistic hypothesis proposed by this study for the three reactions EFE catalyzes. Green dots denote the key branch points. R–H represents the L-Arg substrate.

fate of the ethylene and 3HP formation depends. A recent computational study on the catalytic mechanism of EFE suggested ethylene formation along with forming Fe(II)-pyrocarbonates, claiming an agreement with experimental Mössbauer data.[31] However, the study did not explore the formation of 3HP and the factors responsible for the second branching.[31] Hence, it is important to understand this reaction mechanism and define the second branch point of the EF pathway that diverges to ethylene and 3HP production.

Although several proposals have postulated the structural determinants responsible for this unique reactivity, such as the hydrophobic environment lining the 2OG, the effect of L-Arg substrate orientation, and the role of 2OG conformation,[17,19,24,28,29] the mechanism of the unique EFE reactions in ethylene and 3HP production still remains unclear. It is important to understand the nature of the second branch point along the EF pathway and to delineate the factors responsible for diverging reactivities and the reasons for the lower output of 3HP formation in WT EFE compared to ethylene. Recent experimental studies on EFE variant A198L showed improved 3HP formation compared to WT.[24] The effect of this substitution on the conformational dynamics, the second coordination sphere (SCS), and long-range (LR) interactions needs to be understood to define the factors causing improved 3HP production in the A198L EFE variant. Computational simulations have been widely implemented to study the reaction mechanism of non-heme Fe(II)/2OG enzymes,

providing novel insights into the unique reaction mechanism of each enzyme based on molecular dynamics (MD) and quantum mechanics/molecular mechanics (QM/MM) calculations.[32–41] The studies have shown the complex effects of the SCS and LR interactions on the reaction energetics, intermediates, and the overall reaction path.[29,32,42–46] Hence, to determine the second branchpoint of the EFE reaction mechanism and further elucidate the role of SCS and LR residues, we implemented combined MD and QM/MM methods.

2. Methods

2.1 System preparation

The initial structure of EFE was obtained from the crystal structure (PDB ID: 5v2y)[17] with L-Arg, 2OG in an offline fashion (C1 carboxylate of 2OG bound trans to H268), and an Fe(II)-analog Mn(II) from the RCSB protein data bank. A high-quality structure of the actual reactant complex (Fe(II)-complex) has recently become available (PDB: 6vp4);[23] however, overlaying it with the Mn(II) complex structure (PDB ID: 5v2y)[17] showed that the two structures are highly superimposable (RMSD = 0.17 Å); therefore, to maintain consistency with our previous calculations,[29,46,47] we used the 5v2y crystal structure in this study. The obtained structure was remodeled by replacing Mn with Fe and modifying the water molecule attached trans to the H189 to dioxygen (O_2) to represent the offline Fe(III)–$OO^{\bullet-}$ intermediate. The system WT-EFE-Fe(III)–$OO^{\bullet-}$·L-Arg (**WT-EFE**) thus obtained has Fe with bidentate coordination to 2OG and monodentate coordination to two histidines H189 and H268 and an aspartate D191. The parameters for L-Arg and 2OG were obtained using the generalized Amber force field (GAFF)[48] implemented in the antechamber suite in AmberTools20.[49] The metal center parameters at a high spin (HS) Fe(III)–$OO^{\bullet-}$ intermediate level, including bond and angle force constants, were obtained using the Metal Center Parameter Builder (MCPB.py v3.0)[50] of AmberTools20. The remaining protein residues were modeled using an Amber ff14SB force field.[51] The Na^+ counter ions were added to the system for neutralization using a leap module in Amber20.[49] Finally, the protein system was solvated with TIP3P[52] water molecules, extending up to 10 Å from the farthest point of the protein surface. For the A198L variant, the alanine residue at the 198th position was replaced by a leucine residue using the Chimera tool.[53] The same procedure was repeated for the variant to obtain the A198L-EFE-Fe(III)–$OO^{\bullet-}$·L-Arg (**A198L-EFE**) system. Similarly, the system was modified accordingly for the **EFIV** intermediate, and the parameters were obtained using the MCPB techniques mentioned above. The **EFIV** intermediate for WT EFE (**WT-EFE-EFIV**) and A198L variant (**A198L-EFE-EFIV**) systems were obtained using the same procedure for further calculations.

2.2 Molecular dynamics simulations

Initially, the solvated systems were minimized in two steps. First, the solvent molecules were minimized for 10 000 steps with a restraint of 100 kcal mol^{-1} on the solute molecules. Following this, the whole system was minimized for 10 000 steps. The minimizations were first carried out using the steepest descent (5000 steps) and then the conjugate gradient (5000 steps) method. The systems were then subjected to controlled heating under NVT ensemble from 0 to 300 K using a Langevin thermostat[54,55] with a collision frequency of 1 ps^{-1} for 250 ps with mild restraint using a harmonic potential of 50 kcal mol^{-1} $Å^2$ on the solute molecules. The periodic boundary conditions were implemented in all simulations. Long-range electrostatic interactions were calculated with the particle mesh Ewald method[56,57] with a direct space and van der Waals cutoff of 10 Å. The SHAKE[58] algorithm was used to constrain the bonds involving hydrogens. Following heating, the system undergoes MD simulation for 1 ns to achieve a uniform density with a weak restraint on the solute molecules using periodic boundary conditions. Subsequently, the systems were equilibrated for 3 ns at 300 K in an NPT ensemble without restraint. During the simulations, the pressure was maintained at 1 bar using the Berendsen barostat.[59] The production simulations were performed for 1 μs each with a timestep of 2 fs in an NPT ensemble with pressure set at 1 bar and a constant pressure coupling of 2 ps. The GPU version of Amber20 was used for the production simulations.[49] The hydrogen bond analysis was carried out using the CPPTRAJ[60] module of Amber20. The principal component analysis (PCA) and dynamic cross-correlation analysis (DCCA) were performed on the backbone atoms on the equilibrated portion of the production simulation using the Bio3D[61] module in the R programming language.

2.3 QM/MM simulations

Representative snapshots from the equilibrated regions of the 1 μs MD trajectory were obtained for QM/MM calculations. Water molecules beyond 12 Å from each atom on the protein surface were truncated. QM/MM simulations were conducted using the ChemShell program:[62] DL_POLY[63] for the MM implementation and Turbomole[64] for the QM region. The polarizing effect of the protein environment on the QM region was accounted for using an electrostatic embedding scheme.[65] Hydrogen link atoms were used to cap the QM/MM boundaries using a charge shift model.[65] The facial triad residues (H189, D191, and H268) with Fe, 2OG, and L-Arg substrates defined the QM regions for WT and A198L EFE systems. In the case of **EFIV** systems, the **EFIV** intermediate with the facial triad residues, 2OG, L-Arg, and a water molecule near Fe was included in the QM region. The protein region within 8 Å from the QM region was defined as the flexible MM region, and the rest of the system beyond 8 Å was fixed. The Amber ff14SB forcefield was used for the MM region.[51] Experimental studies demonstrated a quintet spin state as the ground state for non-heme Fe enzymes.[66] Multiple computational studies on the O_2 activation reaction in non-heme Fe(II)/2OG-dependent enzymes have shown that although triplet, quintet, and septet spin states are possible, the reaction proceeds through the HS quintet state.[20,41,67–70] Hence, we used the HS quintet spin state of EFE-Fe(III)–$OO^{\bullet-}$·L-Arg for our reaction path calculations. The geometry optimization and frequency calculations used the def2-SVP[71] basis set with the DFT-B3LYP (QM(B1)/MM) method. The potential energy surface

(PES) scans with specific reaction coordinates for the reaction under study were implemented on the optimized reaction complexes (RCs) with a step size of 0.1 Å to obtain transition states (TSs), intermediate (IM), and product complexes (PCs). Without any constraints, the highest energy points along the PES are optimized using the dimer method[72] implemented in the DL-FIND[73] optimizer. Frequency calculations were performed to confirm the minima and transition states. To further refine the energies, single point (SP) energy calculations were performed on the optimized geometries using a large all-electron def2-TZVP[71] basis set (QM(B2)/MM). The zero-point energies from frequency calculations were added to B2 energy to obtain zero-point corrected QM(B3)/MM energies. The results are discussed at the QM(B3)/MM level of energies. Additionally, we calculated SP energy on the QM/MM geometries of the stationary points with different functionals, including GGA functionals such as PBE and B97-D and double hybrid functionals such as B2-PLYP. The calculations revealed that although the performance of the different functionals varies, the energies obtained at B97-D are closer to those at B3LYP (Tables S1–S3†). The QM/MM method with the B3LYP functional implemented in this study has been widely used[29,42,74–76] and proven efficient in identifying important intermediates along the EFE reaction pathway,[29] including succinyl-peroxo-carbonato-Fe(II) (**EFI**), which was later proven by experimental studies.[28] Natural Orbital (NO) and Spin Natural Orbital (SNO) analyses were carried out using the Gaussian 16 package.[77] The coordinates of the QM/MM optimized structures with the absolute energies obtained during the simulations are given in the ESI.†

3. Results and discussion

3.1 How is ethylene formed? From the propion-3-yl radical or EFIV intermediate?

Despite several experimental and computational efforts,[17–20,24,29,78] how ethylene is formed from 2OG is still unknown. Bollinger *et al.* proposed the formation of an unusual **EFIV** intermediate (Fig. 2b), which undergoes a Grob-like fragmentation to form ethylene or partial fragmentation to form 3-hydoxypropionate.[24,28] To understand the feasibility of this mechanism, we carried out QM/MM calculations on two snapshots obtained from MD simulations of the **WT-EFE** system.[29] MD simulations of the **WT-EFE** system were already discussed in our previous study.[29] We chose the two snapshots considering the closer orientation of SCS residues surrounding the 2OG co-substrate, which was experimentally shown to influence reactivity.[24]

3.1.1 How does the propion-3-yl radical lead to ethylene formation? Initially, we obtained a structure from **WT-EFE** MD simulations and optimized it to get reactant complex 1 (**WT1-RC**). The initial distances between atoms involved in the reaction at **WT1-RC** are as follows: between distal oxygen (O_d) of superoxide and C2 carbon of 2OG it is 2.40 Å, between proximal oxygen (O_p) of superoxide and C1 carbon of 2OG it is 3.11 Å and the O_p–O_d bond distance is 1.27 Å (Fig. 3). The nucleophilic attack of O_d on the C2 carbon of 2OG was carried out using the reaction coordinate involving the approach of distal oxygen (O_d) of dioxygen to C2 carbon of 2OG (O_d–C2) and the increase in the distance of proximal oxygen (O_p) and O_d (O_p–O_d). **WT1-RC** initiates the EF pathway by forming the succinyl-peroxo-carbonato-Fe(II) intermediate (**WT1-EFI**) with a 7.9 kcal mol^{-1} activation barrier through a transition state **WT1-TS1**. At **WT1-TS1**, the O_d–C2 distance is reduced to 1.43 Å, resulting in O_d–C2 bond formation with a distance of 1.36 Å at **WT1-EFI**. During this transformation, the C1–C2 bond of 2OG increases from 1.55 Å to 2.91 Å, resulting in decarboxylation and recombination with O_p with an O_p–C1 bond distance of 1.51 Å at **WT1-EFI**. The formed **WT1-EFI** further undergoes homolytic O_p–O_d bond cleavage to form carbonato-Fe(III) and a succinyl radical (**WT1-EFII**) (Fig. 3). **WT-EFII** undergoes C2–C3 bond breakage through a transition state **WT1-TS3**, which is 8.6 kcal mol^{-1} higher in energy than **WT1-EFII**, which gave a propion-3-yl radical intermediate from the PES scan. However, free optimization of this intermediate led to ethylene (**WT1-ethylene**), indicating a barrierless breakage of the C4–C5 bond. The spin density analysis corroborates the formation of succinyl and propion-3-yl radicals with −0.57 spin density of O_d as part of the succinyl radical in **WT1-EFII** and −0.84 spin density at C3 carbon of the propion-3-yl group in **WT1-TS3** (Fig. S1†).

We could not optimize a stable propion-3-yl radical derived from the WT1 snapshot. Subsequent breakdown of the propion-3-yl radical to ethylene could be correlated with the reduced hydrophobic interactions surrounding the radical in **WT1-EFII** and **WT1-TS3**. For example, L173 has positioned one of its methyl groups away from the C3–C4 bond (Fig. 4). The results suggested that the **EFIV** intermediate might not be required for ethylene formation. All intermediate states identified in the C2–C3 bond breakage PES after **WT1-TS3** converge to ethylene upon free optimization (leading to spontaneous breakage of the C4–C5 bond), reinforcing that ethylene formation happens through sequential breakage of the C2–C3 and C4–C5 bonds.

3.1.2 How does the propion-3-yl radical lead to the EFIV intermediate? In an attempt to explore the stability of the propion-3-yl radical further, we obtained another snapshot from the MD simulation of the **WT-EFE** MD (**WT2-RC**) and repeated the reaction path calculations on it. The initial step in the O_2 activation reaction for **WT2-RC** forming the succinyl-peroxo-carbonato-Fe(II) intermediate (**WT2-EFI**) requires an activation barrier of 6.3 kcal mol^{-1} (Fig. 5a), which subsequently leads to the generation of carbonato-Fe(III) and a succinyl radical (**WT2-EFII**) through O_p–O_d bond breakage. The spin density of O_d oxygen is −0.52 in **WT2-EFII** (Fig. S2†).

The **WT2-EFII** intermediate undergoes a C2–C3 bond cleavage, resulting in a stable propion-3-yl radical (**WT2-EFIII**) with an associated 20.3 kcal mol^{-1} barrier, which is higher compared to **WT1-EFII** C2–C3 bond breakage (8.6 kcal mol^{-1}). At **WT2-EFIII**, the spin density of C3 carbon is −0.94, representing the presence of a radical (Fig. S2†). The stability of the propion-3-yl radical **WT3-EFIII** could be attributed to the hydrogen bonding and hydrophobic interactions with the SCS residues. At the **WT2-EFII** and **WT2-TS3** states, we could see strong salt bridge interactions between the C5 carboxylate and R277 guanidino group, and there are increased hydrophobic

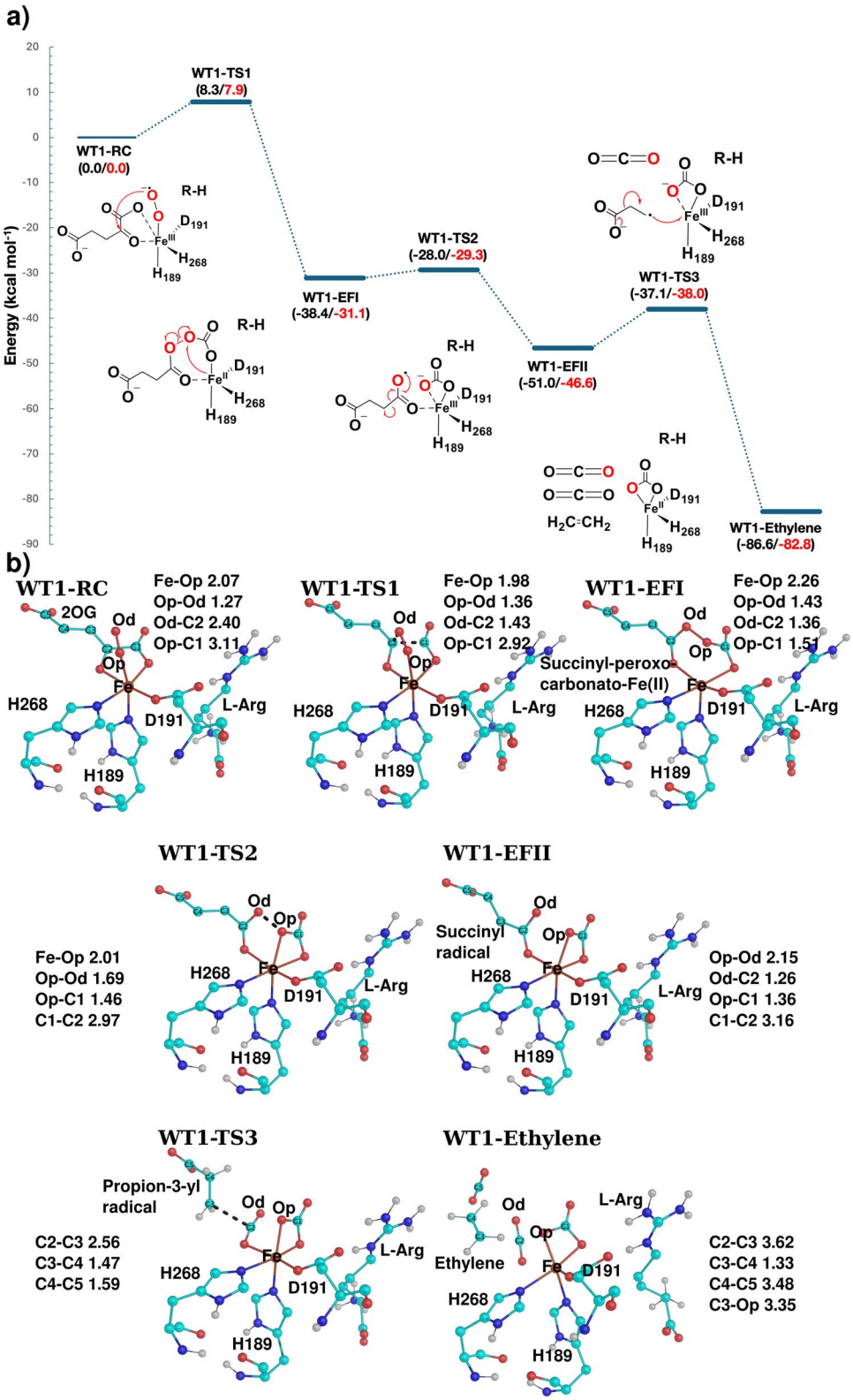

Fig. 3 (a) Reaction profile of the O_2 activation mechanism from the WT1 snapshot. Relative energies are given in kcal mol^{-1} at QM(B2)/MM (black) and QM(B3)/MM (red) levels. The profile was plotted at QM(B3)/MM levels. (b) Representations of QM/MM optimized structures obtained during the O_2 activation mechanism from the EFE WT1 snapshot. Non-polar hydrogens are hidden for clarity. Distances are mentioned in Å.

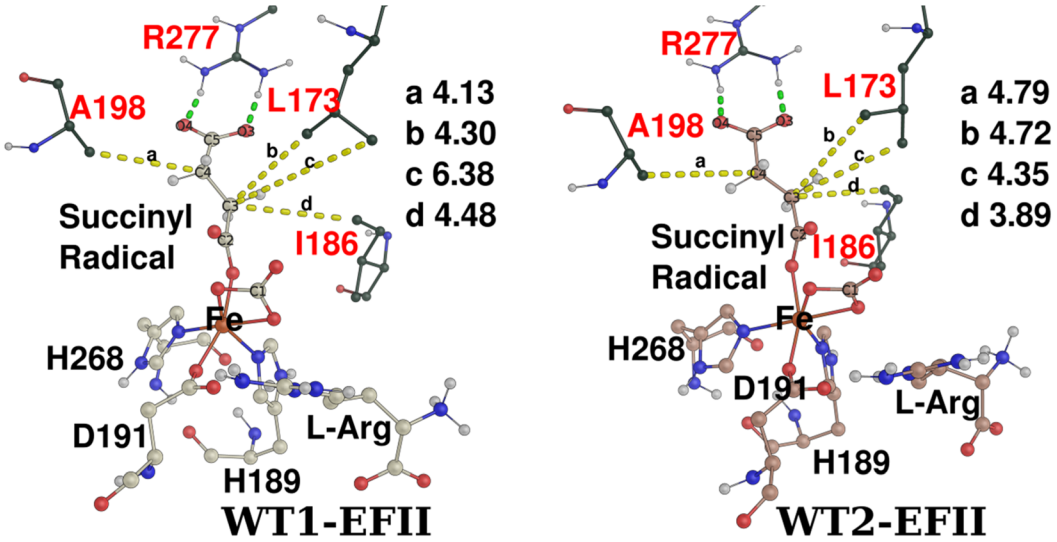

Fig. 4 SCS interactions around the succinyl radical EFII in **WT1-EFII** (left) and **WT2-EFII** (right). Distances are denoted by the yellow dashed line and labeled in Å, and salt bridge interactions are denoted by the green dashed line. Active site residues are labeled in black, and SCS residues in red. Non-polar hydrogens are hidden for clarity.

interactions from L173 along the C3–C4 bond (Fig. 4). Contrary to **WT1-EFII**, both the δ1 and δ2 methyl groups of L173 face toward the C3–C4 bond in **WT2-EFII** and **WT2-TS3**. To explore the reactivity of the propion-3-yl radical, we performed QM/MM reaction path calculations using **WT2-EFIII**. Upon reducing the distance between the C3 carbon of the propion-3-yl radical and the O_p atom of Fe(II)-carbonate, the propion-3-yl radical led to barrierless formation of ethylene (**WT2-ethylene**), which later rebinds to form the (2-carboxyethyl)carbonato-Fe(II) intermediate (**WT2-EFIV′**) with a barrier of 22.6 kcal mol^{-1} (calculated from **WT2-ethylene**) (Fig. S3a†).

To obtain **WT2-EFIV** directly from **WT2-EFIII**, we performed reaction path calculations with a modified reaction coordinate that included a slight restraint on the C4–C5 bond to prevent bond breakage that would lead to ethylene. This approach eventually formed **WT2-EFIV** with a 1.7 kcal mol^{-1} barrier (Fig. 5a). We, therefore, propose that the competition between C4–C5 bond breakage and C3–O_p bond creation (coupling) determines the product distribution between ethylene and 3HP. Fig. 5b shows the optimized structures obtained during the O_2 activation mechanism in WT2. We predict that **WT2-EFIV** may serve as a precursor for 3HP, and the formation of the **EFIV** intermediate determines the yield of 3HP. For comparison, the overlaid reaction profiles of WT1 and WT2 are given in the ESI (Fig. S4†).

However, our attempts to obtain 3HP from **WT2-EFIV** through direct C1–O_p bond cleavage did not yield a product, indicating that a different mechanism is involved in the breakdown of **EFIV** to 3HP. Although our analysis suggests that ethylene is generated in competition with **EFIV**, we considered that it is important to assess whether ethylene formation might also be energetically feasible directly from **EFIV**, as this was proposed by Bollinger *et al.*[24] Consequently, exploring ethylene formation from **WT2-EFIV** indicated that, although ethylene can be produced (**WT2-ethylene′**), the process could be unfeasible due to the high barrier of approximately 57.2 kcal mol^{-1} (Fig. S3b†).

Hence, based on our QM/MM calculations on two snapshots of WT EFE, we hypothesize that ethylene is directly formed from the breakage of the C2–C3 bond and C4–C5 bond sequentially. In contrast, a stabilized propion-3-yl radical might bind with carbonato-Fe(III) to form an **EFIV** intermediate, which, upon further reaction, leads to a 3HP product in agreement with the experimental reports.[24,28] From the present calculations, the formation of ethylene from **EFIV** looks unlikely. However, the mechanism of 3HP formation from **EFIV** still needs to be explored.

3.1.3 Role of SCS interactions in defining the reaction specificity of EFE. Several studies have explored the role of SCS and LR interactions in Fe(II)/2OG enzymes.[32,43–45,75,79–81] The intricate effects of SCS and LR residues lead to substantial changes in product distribution, reaction selectivity, and specificity.[32] Hence, it is crucial to understand the impact of these residues in the EFE in achieving the different reactivities discussed in the above sections. The steric factors surrounding the succinyl radical in **WT1-EFII** and **WT2-EFII** define the process of C2–C3 bond breakage. The hydrophobic interactions provided by the residues A198, L173, and I186 determine the breaking of the succinyl radical in affecting the formation of subsequent reactivities. In **WT1-EFII**, the δ1- and δ2-methyl groups of L173 and the δ-methyl group of I186 (4.48 Å) are respectively at 4.30 Å, 6.38 Å and 4.48 Å distances from the C3 carbon of the succinyl radical facilitating breakdown of the succinyl radical. This breakdown led to the propion-3-yl radical, which subsequently rearranges to form ethylene (Fig. 4). Contrastingly, in **WT2-EFII**, the δ1- and δ2-methyl groups of L173 (4.72 Å and 4.35 Å) and the δ-methyl group of I186 (3.89 Å) are closer to the C3 carbon of the succinyl radical, preventing the radical's dissociation to

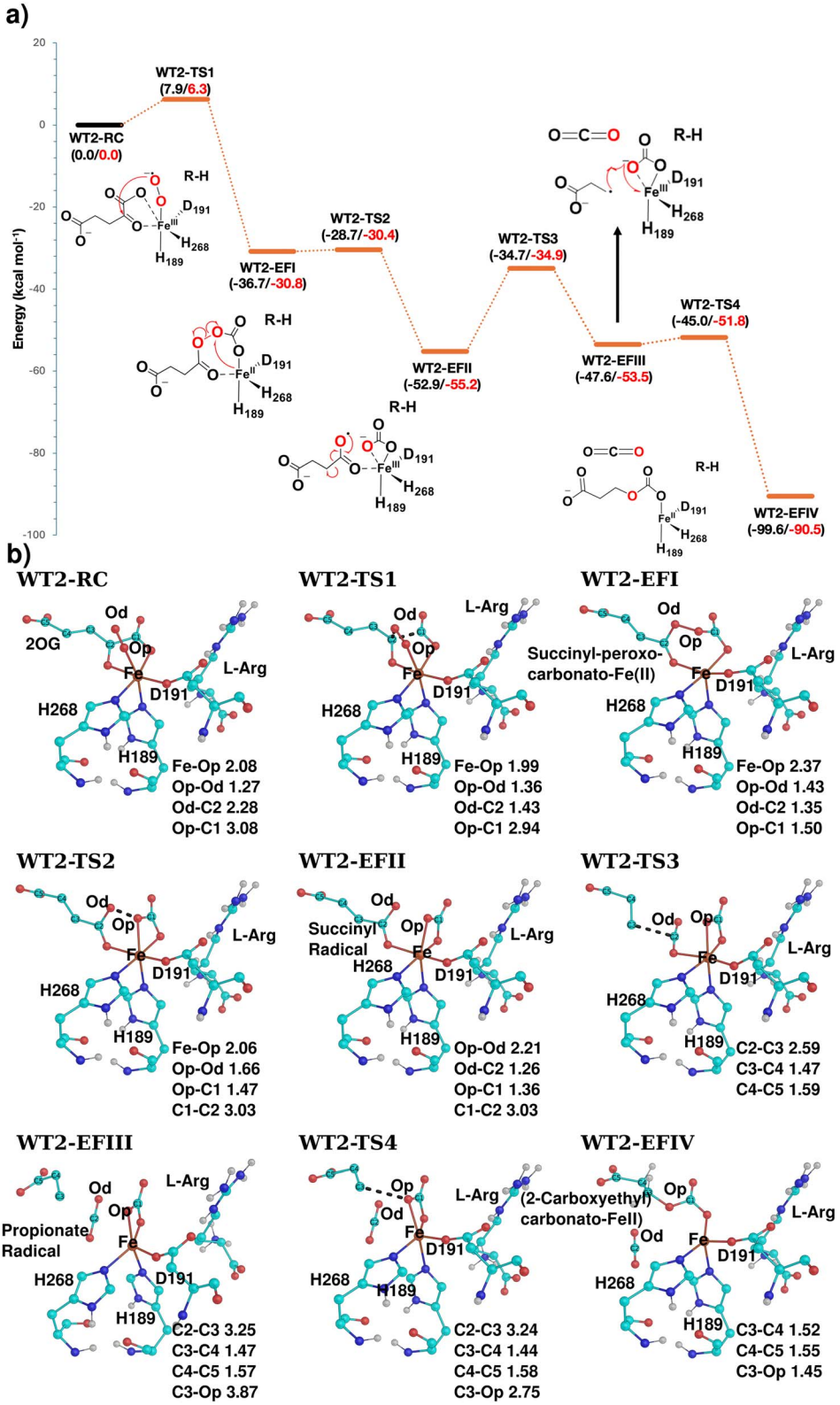

Fig. 5 (a) Reaction profile of the O_2 activation mechanism from the WT2 snapshot. Relative energies are given in kcal mol^{-1} at QM(B2)/MM (black) and QM(B3)/MM (red) levels. The profile was plotted at QM(B3)/MM levels. (b) Representations of QM/MM optimized structures obtained during the O_2 activation mechanism from the EFE WT2 snapshot. Non-polar hydrogens are hidden for clarity. Distances are mentioned in Å.

ethylene (Fig. 4). These hydrophobic interactions stabilize the propion-3-yl radical in **WT2-EFIII**, which combines with carbonato-Fe(III) to form an **EFIV** intermediate. Furthermore, we implemented an EDA analysis to understand the energetic contributions of the SCS and LR residues to important conversions during the EFE catalysis. We found that during C2–C3 bond cleavage of the succinyl radical in **WT1-EFII**, the residues R171, R174, and A279 are involved in the energetic stabilization of the bond-breakage transition state (**WTI-TS3**), whereas E94, A199, and L206 residues are involved in its destabilization (Fig. S5†). R171 forms hydrogen bonding interactions with the C1-derived carbonate group and L-Arg guanidium group, while the residues A199, L206, and A279 form the hydrophobic environment surrounding the succinyl radical. R174 and E94 are found on the surface of the protein. Similarly, the C2–C3 bond breakage in **WT2-EFII** and the R171, R174, and D253 residues provide energetic stabilization to the transition state of this conversion, while D91, E94, and L206 residues cause destabilization (Fig. S6†). D253 makes a hydrogen bond with Fe-coordinated D191, while D91 is part of the L-Arg binding pocket. Notably, the hydrophobic region around the 2OG uniquely stabilizes the propion-3-yl radical formed during catalysis.

3.1.4 Electronic structure analysis of WT EFE snapshots. The reactant complexes (**WT1-RC** and **WT2-RC**) contain the Fe(III)-superoxo complex in a high spin state ($S = 5/2$), which exhibits antiferromagnetic coupling between the Fe(III) center and the superoxo anion radical ($S = 1/2$). The electronic structure analysis of the Fe center in **WT1-RC** predicted an electronic configuration of $^{\uparrow}d_{yz}{}^{\uparrow}d_{xy}{}^{\uparrow}d_{xz}{}^{\uparrow}d_{x^2-y^2}{}^{\uparrow}d_{z^2}{}^{\uparrow\downarrow}\pi^{*\downarrow}_{\parallel}\pi^{*}_{\perp}$ in which the superoxo anion radical is present in the $\pi^{*}_{\perp}$ orbital (Fig. S7†), whereas, in **WT2-RC**, the electronic configuration of $^{\uparrow}d_{yz}{}^{\uparrow}d_{xy}{}^{\uparrow}d_{xz}{}^{\uparrow}d_{x^2-y^2}{}^{\uparrow}d_{z^2}{}^{\uparrow\downarrow}\pi^{*}_{\perp}{}^{\downarrow}\pi^{*}_{\parallel}$ shows that the radical is present in the $\pi^{*}_{\parallel}$ orbital (Fig. S8†). Previous computational studies suggested that the EF pathway is favored irrespective of the presence of the superoxo anion radical in either $\pi^{*}_{\perp}$ or $\pi^{*}_{\parallel}$ orbitals.[29,47] The current calculations also agree with the earlier findings, as **WT1-RC** and **WT2-RC** snapshots followed the EF pathway. The NO and SNO analyses show that the Fe–O_p bond is formed by the orbital overlap of the Fe $d_{x^2-y^2}$ and the $\pi^{*}_{\perp}$ orbitals of O_2 in **WT1-RC**. Conversely, the bonding is achieved by the overlap of Fe d_{xz} and $\pi^{*}_{\parallel}$ orbitals in **WT2-RC**. The transfer of two electrons from the σ_{C1-C2} bond occurs when O_2 attacks C2 of 2OG: one electron to the $\pi^{*}_{\perp}$ orbital and the other to the Fe d_{z^2} orbital in WT1, whereas one electron is transferred to the $\pi^{*}_{\parallel}$ orbital and the other to the Fe $d_{x^2-y^2}$ orbital in WT2. Thus, at **WT1-EFI** and **WT2-EFI**, the electronic configurations are $^{\uparrow}d_{yz}{}^{\uparrow}d_{xy}{}^{\uparrow}d_{xz}{}^{\uparrow}d_{x^2-y^2}{}^{\uparrow\downarrow}d_{z^2}{}^{\uparrow\downarrow}\pi^{*\uparrow\downarrow}_{\parallel}\pi^{*}_{\perp}$ and $^{\uparrow}d_{yz}{}^{\uparrow}d_{xy}{}^{\uparrow}d_{xz}{}^{\uparrow\downarrow}d_{x^2-y^2}{}^{\uparrow}d_{z^2}{}^{\uparrow\downarrow}\pi^{*\uparrow\downarrow}_{\parallel}\pi^{*}_{\perp}$ respectively. Subsequently, the O_p–O_d homolytic cleavage happens with the transfer of a β electron from the Fe d_{z^2} orbital to the σ_{Op-Od} orbital of O_2 in WT1 and from the Fe $d_{x^2-y^2}$ orbital to the σ_{Op-Od} orbital of O_2 in WT2 leading to a succinyl radical and carbonato-Fe(III) in **WT1-EFII** and **WT2-EFII** respectively. The succinyl radical leads to C2–C3 bond breakage by transferring an α electron from σ_{C2-C3} to the C2 carboxylate, releasing C2-based CO_2 and leaving the radical on the propion-3-yl group thus formed. This process is consistent in both **WT1-EFIII** and **WT2-EFIII**. However, upon free optimization of **WT1-EFIII**, an α electron from the σ_{C4-C5} combines with the radical present on C3 carbon to form C3–C4-based ethylene. Meanwhile, the β electron from C5 carboxylate moves to the Fe center to form Fe(II)-carbonate. Conversely, the propion-3-yl radical was optimized with a single electron on C3 carbon in **WT2-EFIII**. Upon the close approach of the propion-3-yl radical to the carbonato-Fe(III) in **WT2-TS4**, the radical β electron is transferred to carbonato-Fe(III) to form the (2-carboxyethyl)carbonato-Fe(II) intermediate (**WT2-EFIV**). The electronic structure analysis of WT1 and WT2 suggests that the electronic rearrangement of the propion-3-yl radical determines the formation of either ethylene or the (2-carboxyethyl)carbonato-Fe(II) intermediate.

3.2 Why SCS variant A198L changes the ratio between ethylene and 3HP?

Experimental studies on WT EFE indicate that 3HP was produced in a yield of less than 1%, significantly lower than the yields of ethylene and P5C.[24,28] However, the SCS variant A198L was reported to produce high yields of 3HP (about 58–66%) compared to WT due to the steric bulk provided by the leucine residue, which perturbs the active site to favor 3HP formation over ethylene.[24] To give an atomistic insight into how the A198L variant of EFE increases the production of 3HP, we carried out MD and QM/MM studies.

3.2.1 How does A198L affect the structure and dynamics of EFE? Compared to alanine, the leucine residue contains more hydrophobic methyl groups. To explore the conformational changes effected by this substitution on EFE, we performed MD simulations on the A198L variant (Fig. S9†). The simulations show stable hydrogen bonds between N^{ε} of L-Arg and the carboxylate group of E84 (73% of 1 μs trajectory) and between the guanidine group of L-Arg and Fe-binding D191 (64%). 2OG is stabilized in the active site through a hydrogen bond between its C5 carboxyl group and R277 (90%). Similarly, the C1 carboxyl group of 2OG is stabilized by a stable hydrogen bond with R171. Overall, the hydrogen bonding interactions are congruent with the **WT-EFE** simulations, with the only exception being the hydrogen bond between the backbone of D191 and D253, which is reduced in the case of the A198L variant (37%) compared to WT (80%). The PCA showed that the overall structure is less flexible except for the terminal region of the protein. Interestingly, the flexible regions in the WT EFE[29] show limited motion in the case of the A198L variant (Fig. 6 and S10†). The trend is reflected in DCCA, which shows a substantial loss in correlated/anticorrelated motions found in the WT EFE (Fig. 6). Notably, the anticorrelated motion between (i) β4, β5, and the loops connecting them (residues 80–93) and (ii) β11 and its connecting loops (residues 211–245) has been lost in A198L EFE. Also, the anticorrelated motion between β15 and the loop connecting it to α8 (residues 291–303) and regions (i) and (ii) has been lost. Overall, the anticorrelated motions have been limited in the A198L variant. This could have implications for the differences in the reactivity of the A198L variant compared to WT, as

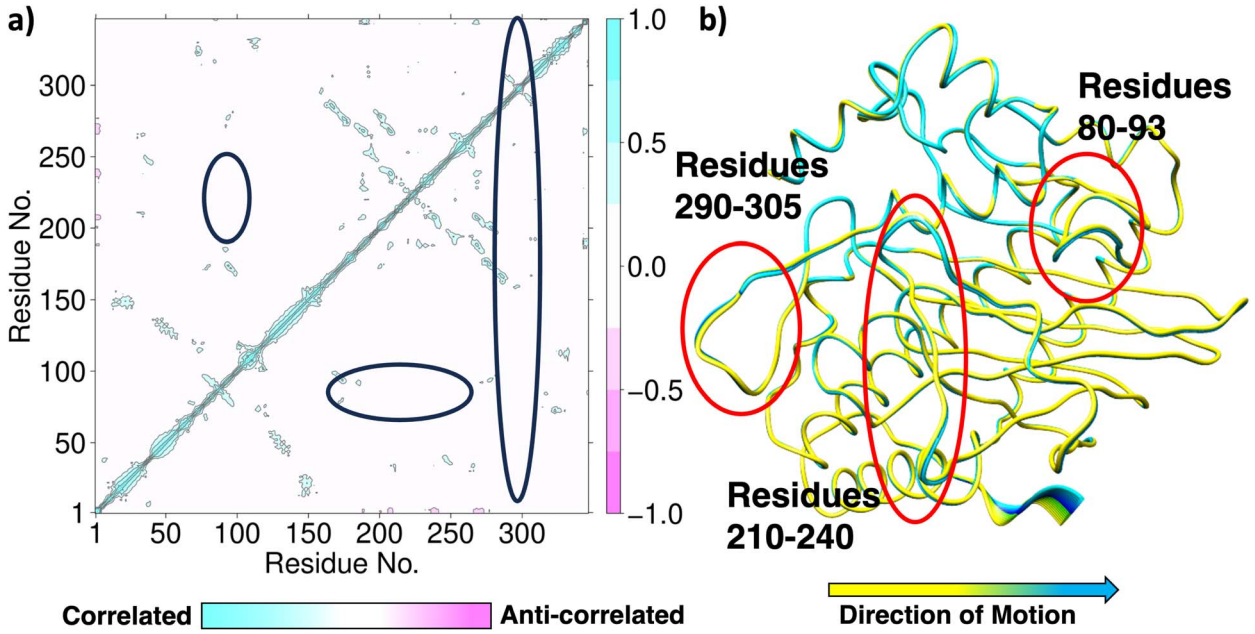

Fig. 6 The overall protein dynamics of **A198L-EFE**. (a) Dynamic cross-correlation matrix shows the regions of correlated and anticorrelated motions in the A198L variant. (b) Principal component analysis shows the flexible regions of the A198L variant. The circled regions show loss of correlated/anticorrelated motion in (a) and flexibility in (b) compared to the **WT-EFE** system.

correlated motions play a significant role in effective catalysis.[61,62]

3.2.2 Mechanism of O_2 activation in the A198L EFE variant. To understand the difference in reactivity of the A198L EFE variant compared to WT EFE, we implemented QM/MM reaction path calculations to explore the complete reaction mechanism. We optimized a representative snapshot from **A198L-EFE** MD simulations to obtain **A198L-RC** and explored the nucleophilic attack of superoxo on the C2 position of 2OG using **A198L-RC**. The interatomic distances are as follows: 2.44 Å between C2 of 2OG and O_d, 1.26 Å between O_p and O_d, and 3.12 Å between C1 of 2OG and O_p, aligning with those observed in the **WT-RCs** (Fig. 7).

The reaction path calculation with the same reaction coordinate as for WT1 led to the energetically favorable EF pathway, forming an Fe(II)-succinyl-peroxy carbonate intermediate (**A198L-EFI**) with a 9.8 kcal mol^{-1} activation barrier (Fig. 7). **A198L-EFI** then undergoes homolytic cleavage of the O_p–O_d bond, forming carbonato-Fe(III) and a succinyl radical (**A198L-EFII**). This succinyl radical intermediate subsequently undergoes C2–C3 bond cleavage, forming a propion-3-yl radical (**A198L-EFIII**) through a barrier of 15.0 kcal mol^{-1}, which then led to the formation of the **EFIV** intermediate (**A198L-EFIV**) with an activation barrier of 1.3 kcal mol^{-1}. The presence of succinyl and propion-3-yl radicals at **A198L-EFII** and **A198L-EFIII**, respectively, is confirmed by the spin density analysis shown in Fig. S11.†

The analysis of the SCS interactions shows that the two methyl groups of the substituted residue L198 form hydrophobic interactions with the C4 carbon of the succinyl radical (3.76 Å and 3.72 Å) in **A198L-EFII**. Similarly, the residues L173 and I186 also form hydrophobic interactions with the C3 carbon of the succinyl radical. Like **WT2-EFII**, these interactions help stabilize propion-3-yl radical formation and the subsequent approach of this radical to carbonato-Fe(III) to form **A198L-EFIV**. However, the A198L variant does not require additional restraints for this conversion as in **WT2-EFIII** because the additional methyl groups of L198 provide the necessary steric effects to form **A198L-EFIV** (Fig. 8). Based on EDA analysis, the residues E84, D253, and E285 give energetically stabilizing contributions to **A198L-TS3** for C2–C3 bond breakage. Contrary to WT snapshots, the residues D91, R171, and D201 are involved in destabilizing **A198L-TS3** (Fig. S12†). R171 is involved in hydrogen bonding interactions with C1 carboxylate (of carbonato-Fe(III)) and L-Arg, while E84 has hydrogen bonding with the guanidino group of L-Arg.

To explore if ethylene formation from the propion-3-yl radical is as favored in the **A198L-EFE** variant as in the WT, we performed reaction path calculation starting from **A198L-EFIII** by increasing the distance between C4 and C5 to facilitate ethylene formation. However, the simulation resulted in an **EFIV** intermediate rather than ethylene, aligning with experimental observations that in the A198L variant, 58–66% of the EF pathway flux is redirected toward the 3HP product. In agreement with the experimental studies,[24] we elucidated that 3HP is formed from the **EFIV** intermediate. The ethylene product is formed with a barrier of 5 kcal mol^{-1} by applying a constraint on the distance between O_p and C3 to prevent bond formation. Hence, the results suggest that ethylene formation is feasible in the A198L mutant, although not as favored as in the WT, and might require further structural rearrangements in the SCS interactions that keep the C3 carbon away from the O_p. The calculations imply that in the **A198L-EFE**

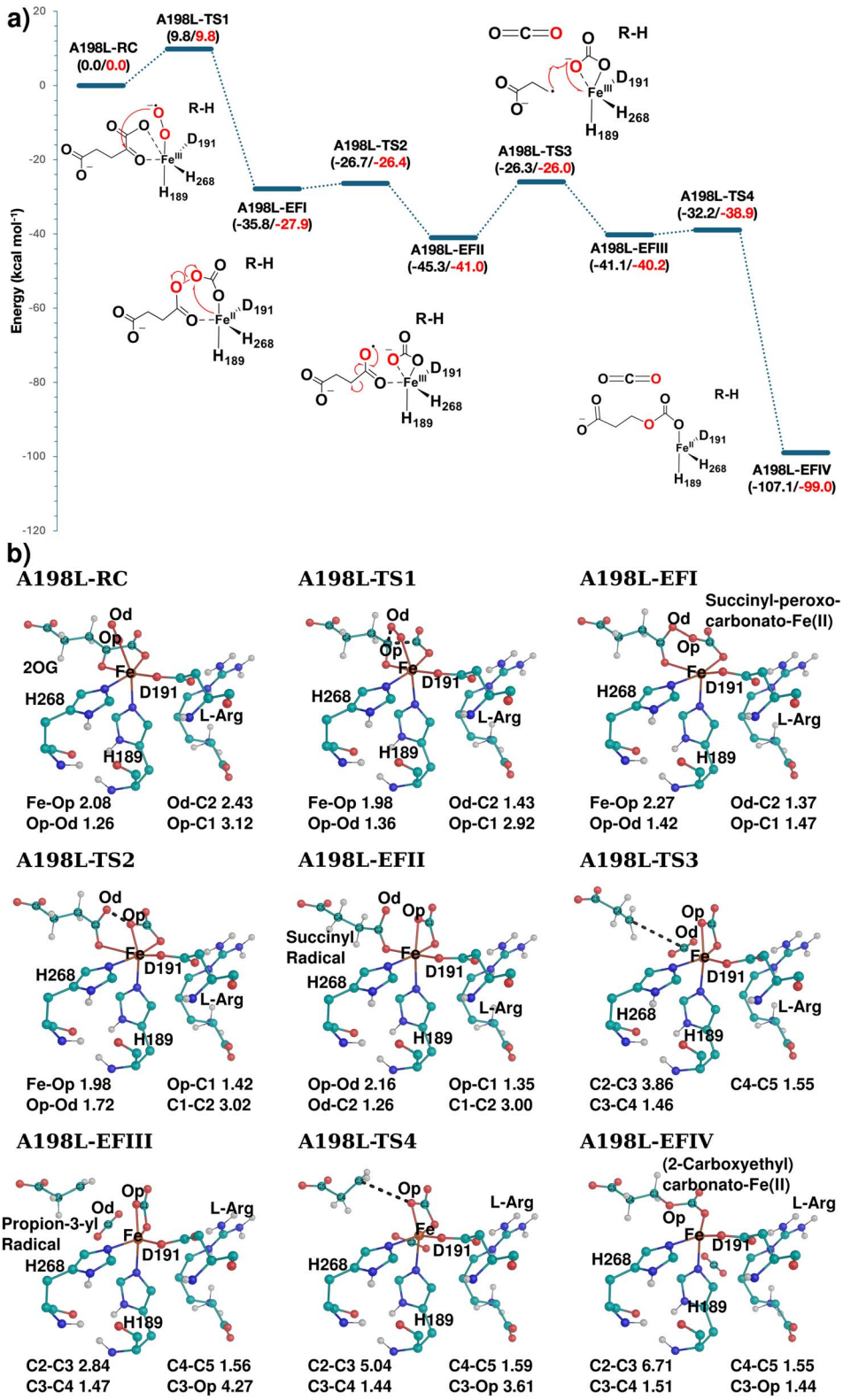

Fig. 7 (a) Reaction profile of the O_2 activation mechanism in the A198L-EFE variant. Relative energies are given in kcal mol^{-1} at QM(B2)/MM (black) and QM(B3)/MM (red) levels. The profile was plotted at the QM(B3)/MM level. (b) Optimized structures obtained during the QM/MM simulations. Distances are mentioned in Å.

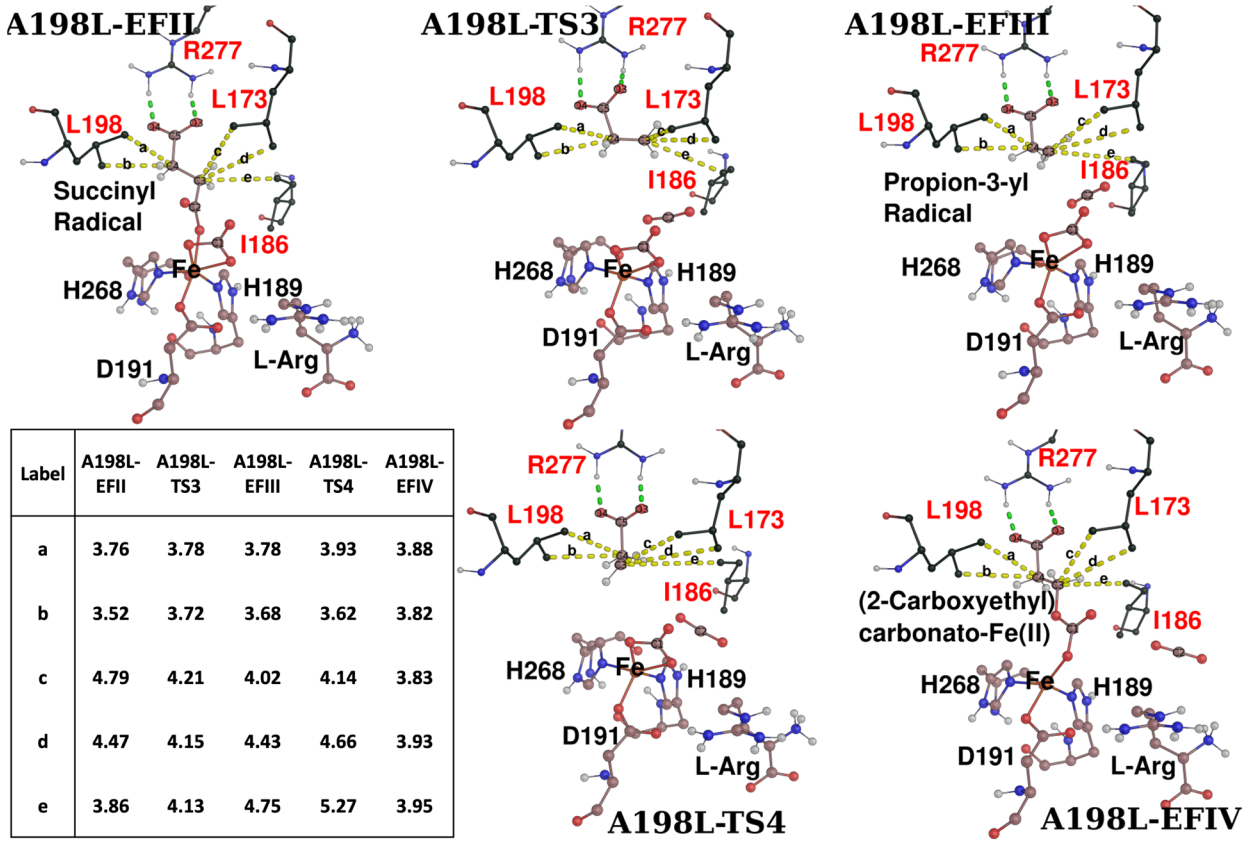

Label	A198L-EFII	A198L-TS3	A198L-EFIII	A198L-TS4	A198L-EFIV
a	3.76	3.78	3.78	3.93	3.88
b	3.52	3.72	3.68	3.62	3.82
c	4.79	4.21	4.02	4.14	3.83
d	4.47	4.15	4.43	4.66	3.93
e	3.86	4.13	4.75	5.27	3.95

Fig. 8 Hydrophobic and salt bridge interactions surrounding the succinyl and propion-3-yl radicals during the formation of EFIV in A198L-EFE. Distances (yellow dashed lines) were tabulated and mentioned in Å. Green dashed lines denote the salt bridge interactions. Non-polar hydrogens were hidden for clarity.

variant, the formation of the **EFIV** intermediate is facilitated compared to WT, thereby increasing the output of 3HP compared to WT EFE. The electronic configuration of **A198L-RC** is $^{1}d_{yz}{}^{1}d_{xy}{}^{1}d_{xz}{}^{1}d_{x^2-y^2}{}^{1}d_{z^2}{}^{1\downarrow}\pi^{*\downarrow}_{\parallel}\pi^{*}_{\perp}$ in which the superoxo anion radical is present in the $\pi^{*}_{\perp}$ orbital (Fig. S13†). The subsequent electronic rearrangement through the successive steps follows the same pathway as the **WT2-RC** pathway.

3.3 Conformational dynamics of the (2-carboxyethyl) carbonato-Fe(II) intermediate in the WT and A198L EFE

The (2-carboxyethyl)carbonato-Fe(II) intermediate is unique for EFE[24,28] as it was not indicated as part of the catalytic mechanism of Fe(II)/2OG-dependent oxygenases. To understand its conformational properties, we performed MD simulations on the **EFIV** intermediate in both WT and A198L variants.

The simulation of the **EFIV** intermediate in WT EFE (**WT-EFE-EFIV**) shows a stable trajectory with an average RMSD of 1.52 Å (Fig. S14†). Compared to the Fe(III)–$OO^{\bullet-}$ dynamics, the L-Arg substrate has moved slightly away from the Fe(II)-center in **WT-EFE-EFIV** simulations (Fig. S15†). Furthermore, the hydrogen bonding analysis of **WT-EFE-EFIV** simulation revealed differences in the hydrogen bonding interactions of the L-Arg substrate. Notable changes include the lower stability (22%) of hydrogen bonding interactions between N^{ε} of L-Arg and D191 carboxylate compared to WT-Fe(III)–$OO^{\bullet-}$ dynamics (64%). This loss in hydrogen bonding interaction leads to the slight movement of L-Arg away from the Fe(II) center. This observation could be attributed to the lack of the role of L-Arg in the **EF** pathway. Also, the carbonate group of the **EFIV** intermediate forms stable hydrogen bonding interactions with the guanidino group of Arg171 (28%). Also, we analyzed the 1 μs trajectory and observed that the water molecules often approach the Fe(II) center. Based on histogram analysis, more than 60% of the snapshots in the trajectory have at least one water molecule within 5 Å from the Fe(II) center (Fig. S16†). This is brought about by the slight displacement of the L-Arg substrate, allowing water molecules to access the Fe center. Based on this intriguing observation, we hypothesize that the further breakdown of the **EFIV** intermediate might involve the role of water molecules, possibly as proton donors.

We further implemented DCCA analysis to understand the LR correlated/anticorrelated interactions at the **EFIV** intermediate state. **EFIV** dynamics revealed loss of correlated and anticorrelated motions predominant in Fe(III)–$OO^{\bullet-}$. The **EFIV** intermediate attached to the Fe center exhibited highly correlated motion with the other Fe-coordinated residues. The regions, including residues 80–93, 210–240, and 290–305, have limited correlated and anticorrelated motion with each other (Fig. S17†). The PCA analysis also showed a loss in the flexibility of these regions compared to WT-Fe(III)–$OO^{\bullet-}$ (Fig. S17†).

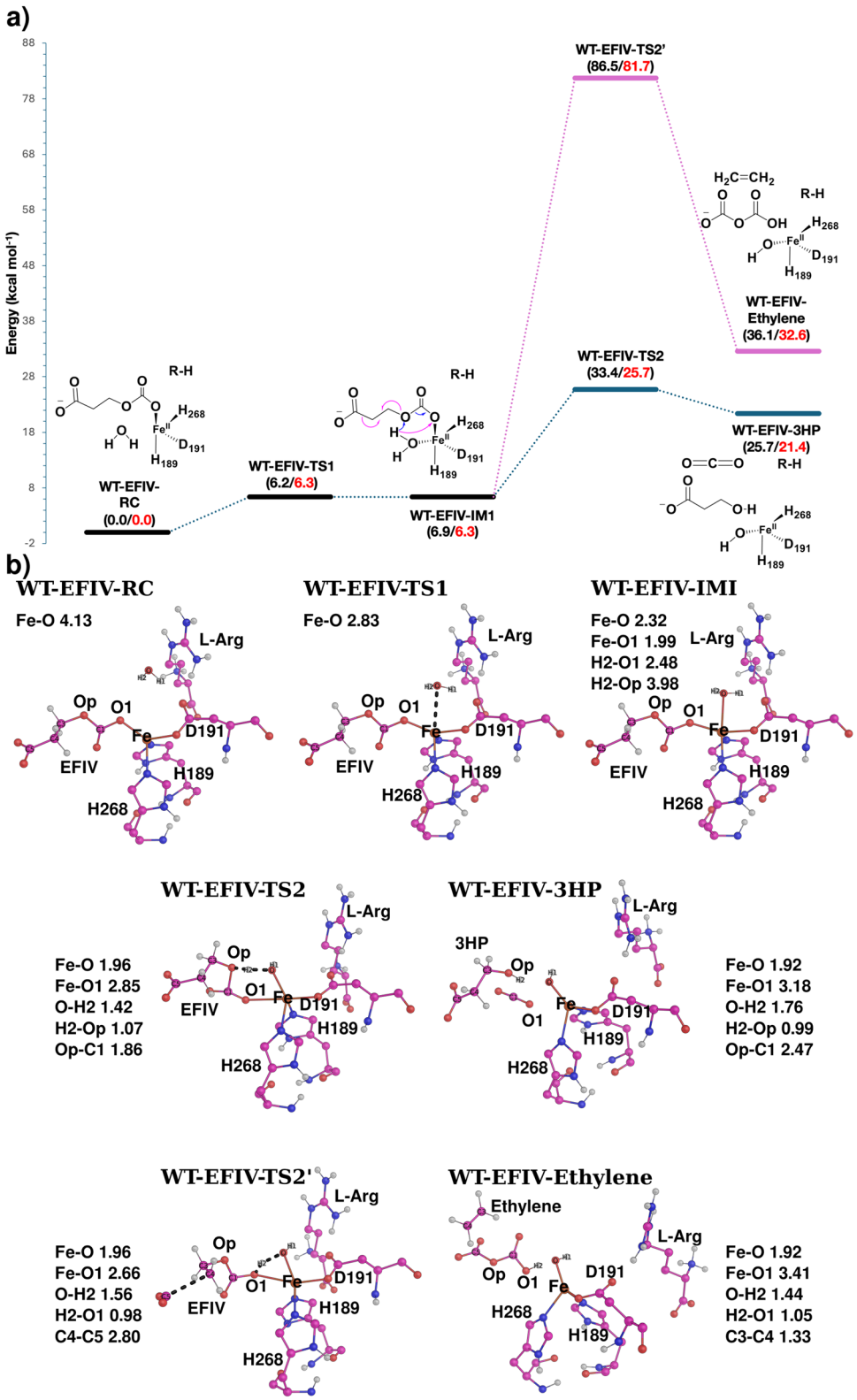

Fig. 9 (a) Reaction profile of 3HP formation in the WT-EFE-EFIV system. Relative energies are given in kcal mol^{-1} at QM(B2)/MM (black) and QM(B3)/MM (red) levels. The profile was plotted at QM(B3)/MM levels. The pink arrow indicates electron movement in ethylene formation, and the blue indicates electron movement in 3HP formation. (b) The optimized geometries of the intermediates and transition states obtained during the QM/MM simulations.

These regions influence the substrate binding and are involved in the hydrophobic region surrounding the **EFIV** intermediate. This apparent change in the flexibility and the correlated motions could be related to the active site change and corresponding LR conformational changes, allowing the solvent molecules to access the Fe center. Overall conformational dynamics analysis of the **EFIV** intermediate in WT intriguingly revealed that more water molecules have access to the Fe center.

To provide some structural background about the catalytic differences between the WT and A198L EFE forms, we explored the conformational dynamics of the **EFIV** intermediate in the A198L variant (**A198L-EFE-EFIV**) (Fig. S18†). Similar to **WT-EFE-EFIV**, the hydrogen bonding interactions between N^{ε} of L-Arg and D191 carboxylate are less prominent in **A198L-EFE-EFIV**. The C5 carboxylate of the **EFIV** intermediate forms stable hydrogen bonding interactions with the guanidino group of R277, similar to the **WT-EFE-EFIV** system and WT Fe(III)–$OO^{\bullet-}$ system. Interestingly, the hydrogen bonding between R171 and the carbonate group of **EFIV** is relatively more stable (33%) than that in **WT-EFE-EFIV**. We also observe the approach of solvent molecules to the Fe center (within 5 Å), which is observed in more than 60% of the trajectory, similar to the **WT-EFE-EFIV** system (Fig. S19†). This observation reiterates the intriguing nature of the **EFIV** intermediate, which allows water molecules to access the Fe(II) center.

DCCA analysis shows that the correlated motions observed in **WT-EFE-EFIV** and WT Fe(III)–$OO^{\bullet-}$ forms have been lost in the **A198L-EFE-EFIV** form (Fig. S20†). However, there is an increased anticorrelated motion between the region forming β4 and β5 sheets (residues 87–92) and the region forming α8 and α9 (residues 186–202) helices. These regions have the residues involved in substrate stabilization. This observation could be related to the change in the active site with increased solvent access to the active site. The conformational dynamics of **A198L-EFE-EFIV** revealed changes in the SCS interactions and correlated motions, which could help in the reaction involving the breakdown of the **EFIV** intermediate.

3.4 Mechanism of 3HP formation

The breakdown of the **EFIV** intermediate has been proposed to form either ethylene or 3HP. While the conversion of **EFIV** to ethylene is energetically unfavorable, the formation of 3HP from its partial breakdown should be explored further. Direct breakdown of **EFIV** through decarboxylation of C1 carboxylate to 3HP is also not feasible. However, MD simulations of the **EFIV** intermediate in WT and A198L variants show that water molecules can access the Fe(II) center, suggesting the potential role of water in the breakdown of **EFIV**. Previous computational studies have explored the role of water molecules in the formation of ethylene.[20] Participation of water in the catalytic mechanism by binding to the metal center and serving as proton donors was proposed in several enzymes, including isopenicillin N synthase[82] and pterin-dependent hydroxylases.[83] To explore this hypothesis in the case of 3HP formation, we conducted QM/MM simulations to define the reaction mechanism of 3HP formation in WT and A198L EFE variants, with water acting as a proton donor.

3.4.1 Mechanism of 3HP formation in WT EFE. We obtained a representative snapshot from the **WT-EFE-EFIV** MD trajectory where a water molecule is closer to the Fe center and optimized it to obtain **WT-EFIV-RC**. At **WT-EFIV-RC**, the water molecule is at 4.13 Å from the Fe center (Fig. 9). Subsequently, we did a potential energy scan calculation to coordinate the water molecule to the Fe center by decreasing the distance between the Fe and oxygen of the water (O_w) molecule (Fe–O_w). The water molecule gets coordinated to the Fe center with a 6.3 kcal mol^{-1} barrier to form **WT-EFIV-IM1**. The Fe–O_w distance is 2.32 Å at **WT-EFIV-IM1**. From this state, proton transfer occurs from the water molecule to the **EFIV** intermediate with simultaneous release of CO_2 to form 3HP (**WT-EFIV-3HP**) through **WT-EFIV-TS2** with a 19.4 kcal mol^{-1} barrier (Fig. 9). The spin population analysis reveals that the Fe is present in the Fe(II) oxidation state throughout the reaction (Fig. S21†). However, we could see negative charge generation in the OH group of the water molecule (OH_w), confirming the proton transfer from the water to 3HP. Although **WT-EFIV-3HP** is endothermic with an energy of 21.4 kcal mol^{-1} with respect to **WT-EFIV-RC**, compared to the Fe(III)–$OO^{\bullet-}$ intermediate, **WT-EFIV-3HP** is thermodynamically exothermic. We further suppose that H^+ from the solution might help remove the Fe-coordinated OH group as water and form an exothermic product; however, this possibility requires further exploration. Furthermore, to completely rule out the possibility of ethylene formation from **EFIV**, we carried out QM/MM reaction path calculations to form ethylene from **EFIV** with the aid of proton transfer from the water molecule to the carbonate group of the **EFIV** intermediate. As seen in earlier calculations in this study, the current calculations also gave an ethylene product with a high activation barrier of 75.4 kcal mol^{-1} through a transition state **WT-EFIV-TS2′**, reiterating that ethylene formation is not feasible from **EFIV** (Fig. 9).

3.4.2 Mechanism of 3HP formation in A198L EFE. To define the reaction mechanism of 3HP formation in the case of the A198L variant of EFE, we carried out QM/MM optimizations on the snapshot obtained from the **A198L-EFE-EFIV** MD trajectory with a water molecule closer to the active site of A198L EFE. The optimized structure **A198L-EFIV-RC** undergoes the potential energy surface scan to coordinate the water molecule to the Fe center. The coordination of water requires a 14.3 kcal mol^{-1} barrier, which gives **A198L-EFIV-IM2** (Fig. 10). At this state, the distance between Fe and O_w of the water molecule is 2.33 Å. Subsequently, proton transfer occurs between the water molecule and carbonate group of the **EFIV** intermediate with the release of a CO_2 molecule to obtain n 3HP (**A198L-EFIV-3HP**) through an activation barrier of 22.7 kcal mol^{-1}. Although the **A198L-EFIV-3HP** product is endothermic with respect to **A198L-EFIV-RC**, it is less endothermic with 12.4 kcal mol^{-1} energy compared to the 21.4 kcal mol^{-1} energy of **WT-EFIV-3HP**. Hence, the 3HP product in the A198L EFE is more stabilized than WT EFE. Also, it is important to notice that the energy span between **A198L-EFIV-RC** and **A198L-EFIV-TS2** is 26.9 kcal mol^{-1}, comparable to that observed in WT. Like the **WT-EFIV-RC**

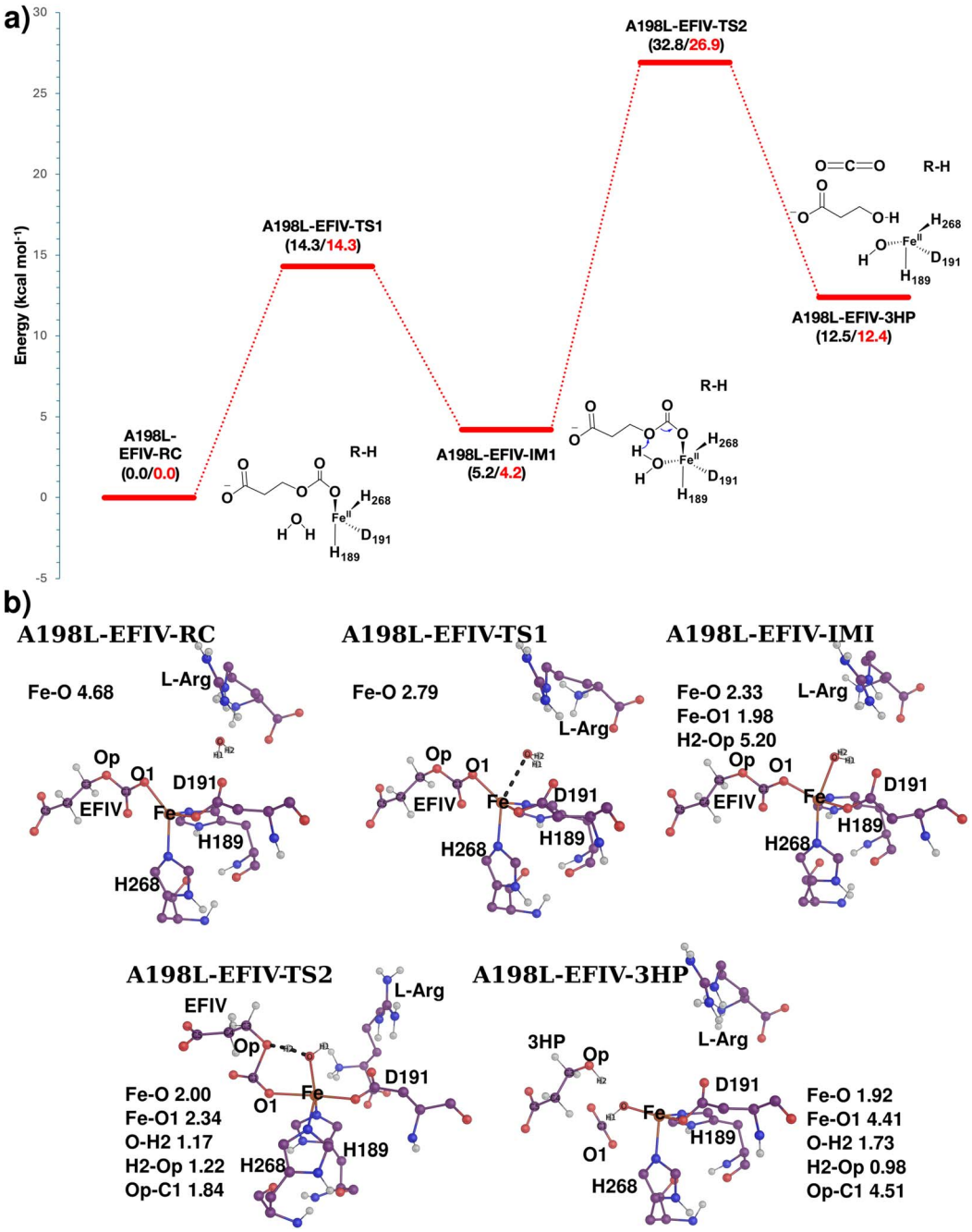

Fig. 10 (a) Reaction profile of the 3HP formation mechanism in A198L EFE. Relative energies are given in kcal mol^{-1} at QM(B2)/MM (black) and QM(B3)/MM (red) levels. The profile was plotted at QM(B3)/MM levels. (b) The optimized geometries of the intermediates and transition states obtained during the QM/MM simulations.

reaction path, the spin population analysis revealed that the Fe center is at Fe(II) oxidation throughout the reaction (Fig. S22†). Contrary to WT, ethylene is not obtained from EFIV in the A198L EFE variant as the energy increases throughout the reaction path calculations without leading to an ethylene product.

3.5 Alternate sources of hydrogen for EFIV breakdown

In addition to the Fe(II)-coordinated water molecule as a proton source, we explored a potential proton transfer from the protonated SCS residues in **EFIV** (Fig. S23†). In particular, we attempted proton transfer from R171 – one of the SCS residues involved in C1 stabilization of 2OG and carbonate stabilization in **EFIV**, as studies suggest that arginine can be involved in proton transfer reactions.[84] Despite several attempts using different combinations of reaction coordinates, the formation of 3HP or ethylene is either not achieved or energetically unfavorable. We also explored proton transfer from a water molecule through the E84 residue, which did not lead to stable products. Additionally, we explored proton transfer from non-coordinated

water molecules, but it did not lead to 3HP or ethylene products. Based on our calculations, Fe(II)-coordinated water can be the viable proton source for forming 3HP.

4. Conclusions

The current study provides a comprehensive account of the mechanism of EFE, particularly the second branch point along the EF pathway, which determines the formation of ethylene and 3HP. We employed combined MD and QM/MM simulations to understand the mechanism. Our primary goal was to describe the EF pathway through conformational analysis of intermediates obtained during the reaction, including the succinyl radical (**EFII**), the propion-3-yl radical (**EFIII**), and the (2-carboxyethyl)carbonato-Fe(II) (**EFIV**) intermediate. We presented the critical conformational and electronic factors related to these intermediates and their outcomes, particularly the hydrophobic environment around 2OG, SCS, and LR residues that govern the stability and fate of these intermediates. Contrary to the previous proposal, we propose a pathway in the EFE reaction mechanism where the second branch point of the EF pathway occurs at the **EFIII** intermediate state instead of **EFIV**.[24,28]

Our simulations suggested that ethylene formation happens through a pathway involving sequential bond breakages of the C2–C3 bond followed by the C4–C5 bond of the succinyl radical through a branch point propion-3-yl radical (**EFIII**) intermediate. QM/MM simulations on two snapshots of the WT EFE system predicted that the competition between C4–C5 bond breakage and C3–O_p bond coupling determines the fate of the **EFIII** intermediate to form ethylene as in WT1, or **EFIII** approaches and binds to carbonato-Fe(III) to form the 2-carboxyethylcarbonato-Fe(II) (**EFIV**) intermediate as in WT2, respectively. The results predicted that the fine-tuning of the hydrophobic SCS residues surrounding the propion-3-yl radical (2OG binding site) plays a key role in stabilizing the propion-3-yl radical. More relaxed hydrophobic SCS interactions surrounding the **EFIII** intermediate lead to its rapid decomposition to ethylene, whereas stable **EFIII** with tighter hydrophobic interactions surrounding it eventually led to the formation of the **EFIV** intermediate. Our efforts to simulate ethylene formation from **EFIV** have not provided any feasible pathway.

We also carried out the QM/MM simulations on the A198L EFE variant, which was experimentally shown to have increased 3HP formation, to verify that 3HP formation comes from **EFIV**. Simulations on the A198L EFE predicted that the variant showed tighter SCS interactions around the propion-3-yl radical, which facilitates the formation of the **EFIV** intermediate. However, the ethylene formation from the propion-3-yl radical in A198L EFE required additional restraints to prevent its bonding with carbonato-Fe(III), suggesting that additional conformational/SCS rearrangement is required in A198L EFE to form ethylene. Furthermore, we propose that the fate of the **EFIII** intermediate dictates the product distribution of ethylene and 3HP.

Moreover, our study explored the **EFIV** intermediate in WT and A198L EFE using MD simulation, which predicted that water molecules, facilitated by enzyme flexibility, can access the Fe(II) center. This provides a rationale for a mechanism where a water molecule bound to the Fe(II) center can act as a proton donor, aiding in 3HP formation. Our QM/MM simulations revealed that the Fe(II)-coordinated water molecules transfer a proton to the **EFIV** intermediate with simultaneous decarboxylation, giving 3HP in both WT and A198L EFE with comparable energies. However, the difference in the product distribution of ethylene and 3HP between WT (approx. 99 : 1) and A198L (approx. 60 : 30) could be attributed to the enhanced facilitation of the **EFIV** intermediate formation in A198L EFE compared to WT.

Overall, our computational study provides important insight into the recent experimental studies[24,28] about the reaction mechanism of EFE, emphasizing the role of the SCS in tuning the reaction product distribution. Thus, the results provided in this study in the longer term can guide future enzyme redesign efforts of EFE for enhanced production of ethylene or 3HP.

Data availability

The data supporting this article have been included in the ESI.†

Author contributions

Conceptualization, C. Z. C.; methodology, C. Z. C. and S. B. J. S. R.; investigation and formal analysis, S. B. J. S. R.; discussion of results S. B. J. S. R., M. G. T., C. Z. C. writing – original draft, S. B. J. S. R. and C. Z. C.; writing – review and editing, S. B. J. S. R., M. G. T., C. Z. C.; visualization, S. B. J. S. R.; funding acquisition, C. Z. C.; supervision, C. Z. C.

Conflicts of interest

There are no conflicts to declare.

Acknowledgements

We thank our collaborators, Prof. Robert P. Hausinger and Prof. Jian Hu from Michigan State University, for the valuable and helpful discussions. This research was supported by the National Science Foundation grant 2203630 to CZC.

References

1 F. B. Abeles, P. W. Morgan and M. E. Saltveit, *Ethylene in Plant Biology*, Elsevier Science, 2012.
2 A. B. Bleecker and H. Kende, *Annu. Rev. Cell Dev. Biol.*, 2000, **16**, 1–18.
3 M. Ghanta, D. Fahey and B. Subramaniam, *Appl. Petrochem. Res.*, 2014, **4**, 167–179.
4 K. M. Sundaram, M. M. Shreehan and E. F. Olszewski, in *Kirk-Othmer Encyclopedia of Chemical Technology*, John Wiley & Sons, Ltd, 2010, pp. 1–39.

5 R. Fluhr, A. K. Mattoo and D. R. Dilley, *Crit. Rev. Plant Sci.*, 1996, **15**, 479–523.
6 D. G. McRae, J. A. Coker, R. L. Legge and J. E. Thompson, *Plant Physiol.*, 1983, **73**, 784–790.
7 J. G. Dong, J. C. Fernández-Maculet and S. F. Yang, *Proc. Natl. Acad. Sci. U. S. A.*, 1992, **89**, 9789–9793.
8 Z. Zhang, J.-S. Ren, I. J. Clifton and C. J. Schofield, *Chem. Biol.*, 2004, **11**, 1383–1394.
9 R. P. Hausinger, S. B. J. S. Rifayee, M. G. Thomas, S. Chatterjee, J. Hu and C. Z. Christov, *RSC Chem. Biol.*, 2023, **4**, 635–646.
10 G. D. Peiser, T.-T. Wang, N. E. Hoffman, S. F. Yang, H. Liu and C. T. Walsh, *Proc. Natl. Acad. Sci. U. S. A.*, 1984, **81**, 3059–3063.
11 T. Ogawa, M. Takahashi, T. Fujii, M. Tazaki, H. Fukuda and J. Ferment, *Bioengineering*, 1990, **69**, 287–291.
12 S. B. Primrose, *J. Gen. Microbiol.*, 1977, **98**, 519–528.
13 K. Nagahama, T. Ogawa, T. Fujii, M. Tazaki, S. Tanase, Y. Morino and H. Fukuda, *Microbiology*, 1991, **137**, 2281–2286.
14 H. Fukuda, T. Ogawa, M. Tazaki, K. Nagahama, T. Fujiil, S. Tanase and Y. Morino, *Biochem. Biophys. Res. Commun.*, 1992, **188**, 483–489.
15 M. Goto, Y. Ishida, Y. Takikawa and H. Hyodo, *Plant Cell Physiol.*, 1985, **26**, 141–150.
16 M. Goto and H. Hyodo, *Plant Cell Physiol.*, 1987, **28**, 405–414.
17 S. Martinez, M. Fellner, C. Q. Herr, A. Ritchie, J. Hu and R. P. Hausinger, *J. Am. Chem. Soc.*, 2017, **139**, 11980–11988.
18 Z. Zhang, T. J. Smart, H. Choi, F. Hardy, C. T. Lohans, M. I. Abboud, M. S. W. Richardson, R. S. Paton, M. A. McDonough and C. J. Schofield, *Proc. Natl. Acad. Sci. U. S. A.*, 2017, **114**, 4667–4672.
19 S. Martinez and R. P. Hausinger, *Biochemistry*, 2016, **55**, 5989–5999.
20 J. Xue, J. Lu and W. Lai, *Phys. Chem. Chem. Phys.*, 2019, **21**, 9957–9968.
21 Md. S. Islam, T. M. Leissing, R. Chowdhury, R. J. Hopkinson and C. J. Schofield, *Annu. Rev. Biochem.*, 2018, **87**, 585–620.
22 R. P. Hausinger, *Crit. Rev. Biochem. Mol. Biol.*, 2008, **39**, 21–68.
23 R. A. Copeland, K. M. Davis, T. K. C. Shoda, E. J. Blaesi, A. K. Boal, C. Krebs and J. M. Bollinger, *J. Am. Chem. Soc.*, 2021, **143**, 2293–2303.
24 E. J. Burke, R. A. Copeland, Y. Dixit, C. Krebs and J. M. Bollinger, *J. Am. Chem. Soc.*, 2024, **146**, 1977–1983.
25 S. Dhingra, Z. Zhang, C. T. Lohans, L. Brewitz and C. J. Schofield, *J. Biol. Chem.*, 2024, **300**, 107546.
26 X.-R. Jiang, X. Yan, L.-P. Yu, X.-Y. Liu and G.-Q. Chen, *Nat. Commun.*, 2021, **12**, 1513.
27 S. S. Chaturvedi, M. G. Thomas, S. B. J. S. Rifayee, W. White, J. Wildey, C. Warner, C. J. Schofield, J. Hu, R. P. Hausinger, T. G. Karabencheva-Christova and C. Z. Christov, *Chem.–Eur. J.*, 2023, **29**, e202300138.
28 R. A. Copeland, S. Zhou, I. Schaperdoth, T. K. C. Shoda, J. M. Bollinger and C. Krebs, *Science*, 2021, **373**, 1489–1493.
29 S. S. Chaturvedi, R. Ramanan, J. Hu, R. P. Hausinger and C. Z. Christov, *ACS Catal.*, 2021, **11**, 1578–1592.
30 C.-C. G. Yeh, S. Ghafoor, J. K. Satpathy, T. Mokkawes, C. V. Sastri and S. P. de Visser, *ACS Catal.*, 2022, **12**, 3923–3937.
31 C. Wang and E. Sayfutyarova, *ChemRxiv*, 2024, DOI: 10.26434/chemrxiv-2024-pz39d.
32 S. P. de Visser, *Chem.–Eur. J.*, 2020, **26**, 5308–5327.
33 H. S. Ali, J. Warwicker and S. P. de Visser, *ACS Catal.*, 2023, **13**, 10705–10721.
34 D. W. Kastner, A. Nandy, R. Mehmood and H. J. Kulik, *ACS Catal.*, 2023, **13**, 2489–2501.
35 R. Mehmood, V. Vennelakanti and H. J. Kulik, *ACS Catal.*, 2021, **11**, 12394–12408.
36 H. Chen, K.-B. Cho, W. Lai, W. Nam and S. Shaik, *J. Chem. Theory Comput.*, 2012, **8**, 915–926.
37 H. J. Kulik and C. L. Drennan, *J. Biol. Chem.*, 2013, **288**, 11233–11241.
38 T. Borowski, H. Noack, M. Radoń, K. Zych and P. E. M. Siegbahn, *J. Am. Chem. Soc.*, 2010, **132**, 12887–12898.
39 K. Dutta Dubey, B. Wang, M. Vajpai and S. Shaik, *Chem. Sci.*, 2017, **8**, 5335–5344.
40 B. Wang, Z. Cao, D. A. Sharon and S. Shaik, *ACS Catal.*, 2015, **5**, 7077–7090.
41 S. Ye, C. Riplinger, A. Hansen, C. Krebs, J. M. Bollinger Jr and F. Neese, *Chem.–Eur. J.*, 2012, **18**, 6555–6567.
42 S. O. Waheed, S. S. Chaturvedi, T. G. Karabencheva-Christova and C. Z. Christov, *ACS Catal.*, 2021, **11**, 3877–3890.
43 R. Ramanan, S. S. Chaturvedi, N. Lehnert, C. J. Schofield, T. G. Karabencheva-Christova and C. Z. Christov, *Chem. Sci.*, 2020, **11**, 9950–9961.
44 S. S. Chaturvedi, S. B. Jaber Sathik Rifayee, S. O. Waheed, J. Wildey, C. Warner, C. J. Schofield, T. G. Karabencheva-Christova and C. Z. Christov, *JACS Au*, 2022, **2**, 2169–2186.
45 S. B. J. S. Rifayee, S. S. Chaturvedi, C. Warner, J. Wildey, W. White, M. Thompson, C. J. Schofield and C. Z. Christov, *Chem.–Eur. J.*, 2023, **29**, e202301305.
46 M. G. Thomas, S. B. Jaber Sathik Rifayee and C. Z. Christov, *ACS Catal.*, 2024, **14**, 18550–18569.
47 S. S. Chaturvedi, S. B. Jaber Sathik Rifayee, R. Ramanan, J. A. Rankin, J. Hu, R. P. Hausinger and C. Z. Christov, *Phys. Chem. Chem. Phys.*, 2023, **25**, 13772–13783.
48 J. Wang, R. M. Wolf, J. W. Caldwell, P. A. Kollman and D. A. Case, *J. Comput. Chem.*, 2004, **25**, 1157–1174.
49 D. A. Case, K. Belfon, I. Y. Ben-Shalom, S. R. Brozell, D. S. Cerutti, T. E. Cheatham, V. W. D. Cruzeiro, T. A. Darden, R. E. Duke, G. Giambasu, M. K. Gilson, H. Gohlke, A. W. Goetz, R. Harris, S. Izadi, S. A. Izmailov, K. Kasavajhala, A. Kovalenko, R. Krasny, T. Kurtzman, T. S. Lee, S. LeGrand, P. Li, C. Lin, J. Liu, T. Luchko, R. Luo, V. Man, K. M. Merz, Y. Miao, O. Mikhailovskii, G. Monard, H. Nguyen, A. Onufriev, F. Pan, S. Pantano, R. Qi, D. R. Roe, A. Roitberg, C. Sagui, S. Schott-Verdugo, J. Shen, C. L. Simmerling, N. R. Skrynnikov, J. Smith, J. Swails, R. C. Walker, J. Wang, L. Wilson, R. M. Wolf, X. Wu, Y. Xiong, Y. Xue, D. M. York and P. A. Kollman, *Amber 2020*, University of California, San Francisco, 2020.
50 P. Li and K. M. Merz, *J. Chem. Inf. Model.*, 2016, **56**, 599–604.

51 J. A. Maier, C. Martinez, K. Kasavajhala, L. Wickstrom, K. E. Hauser and C. Simmerling, *J. Chem. Theory Comput.*, 2015, **11**, 3696–3713.
52 W. L. Jorgensen, J. Chandrasekhar, J. D. Madura, R. W. Impey and M. L. Klein, *J. Chem. Phys.*, 1983, **79**, 926–935.
53 E. F. Pettersen, T. D. Goddard, C. C. Huang, G. S. Couch, D. M. Greenblatt, E. C. Meng and T. E. Ferrin, *J. Comput. Chem.*, 2004, **25**, 1605–1612.
54 R. L. Davidchack, R. Handel and M. V. Tretyakov, *J. Chem. Phys.*, 2009, **130**, 234101.
55 J. Liu, D. Li and X. Liu, *J. Chem. Phys.*, 2016, **145**, 024103.
56 T. Darden, D. York and L. Pedersen, *J. Chem. Phys.*, 1993, **98**, 10089–10092.
57 R. Salomon-Ferrer, A. W. Götz, D. Poole, S. Le Grand and R. C. Walker, *J. Chem. Theory Comput.*, 2013, **9**, 3878–3888.
58 S. Miyamoto and P. A. Kollman, *J. Comput. Chem.*, 1992, **13**, 952–962.
59 G. Bussi, D. Donadio and M. Parrinello, *J. Chem. Phys.*, 2007, **126**, 014101.
60 D. R. Roe and T. E. Cheatham, *J. Chem. Theory Comput.*, 2013, **9**, 3084–3095.
61 B. J. Grant, A. P. C. Rodrigues, K. M. ElSawy, J. A. McCammon and L. S. D. Caves, *Bioinformatics*, 2006, **22**, 2695–2696.
62 S. Metz, J. Kästner, A. A. Sokol, T. W. Keal and P. Sherwood, *WIREs Computational Molecular Science*, 2014, **4**, 101–110.
63 W. Smith, C. W. Yong and P. M. Rodger, *Mol. Simul.*, 2002, **28**, 385–471.
64 S. G. Balasubramani, G. P. Chen, S. Coriani, M. Diedenhofen, M. S. Frank, Y. J. Franzke, F. Furche, R. Grotjahn, M. E. Harding, C. Hättig, A. Hellweg, B. Helmich-Paris, C. Holzer, U. Huniar, M. Kaupp, A. Marefat Khah, S. Karbalaei Khani, T. Müller, F. Mack, B. D. Nguyen, S. M. Parker, E. Perlt, D. Rappoport, K. Reiter, S. Roy, M. Rückert, G. Schmitz, M. Sierka, E. Tapavicza, D. P. Tew, C. van Wüllen, V. K. Voora, F. Weigend, A. Wodyński and J. M. Yu, *J. Chem. Phys.*, 2020, **152**, 184107.
65 M. J. Field, P. A. Bash and M. Karplus, *J. Comput. Chem.*, 1990, **11**, 700–733.
66 S. Hong, K. D. Sutherlin, J. Park, E. Kwon, M. A. Siegler, E. I. Solomon and W. Nam, *Nat. Commun.*, 2014, **5**, 5440.
67 A. R. Diebold, C. D. Brown-Marshall, M. L. Neidig, J. M. Brownlee, G. R. Moran and E. I. Solomon, *J. Am. Chem. Soc.*, 2011, **133**, 18148–18160.
68 D. Fang, R. L. Lord and G. A. Cisneros, *J. Phys. Chem. B*, 2013, **117**, 6410–6420.
69 X. Song, J. Lu and W. Lai, *Phys. Chem. Chem. Phys.*, 2017, **19**, 20188–20197.
70 A. Wójcik, M. Radoń and T. Borowski, *J. Phys. Chem. A*, 2016, **120**, 1261–1274.
71 F. Weigend, *Phys. Chem. Chem. Phys.*, 2006, **8**, 1057–1065.
72 G. Henkelman and H. Jónsson, *J. Chem. Phys.*, 1999, **111**, 7010–7022.
73 J. Kästner, J. M. Carr, T. W. Keal, W. Thiel, A. Wander and P. Sherwood, *J. Phys. Chem. A*, 2009, **113**, 11856–11865.
74 S. S. Chaturvedi, R. Ramanan, N. Lehnert, C. J. Schofield, T. G. Karabencheva-Christova and C. Z. Christov, *ACS Catal.*, 2020, **10**, 1195–1209.
75 R. Ramanan, S. O. Waheed, C. J. Schofield and C. Z. Christov, *Chem.–Eur. J.*, 2021, **27**, 11827–11836.
76 J. Liu, Z. Wang, X. Sang, X. Zhang and B. Wang, *ACS Catal.*, 2023, 5808–5818.
77 M. J. Frisch, G. W. Trucks, H. B. Schlegel, G. E. Scuseria, M. A. Robb, J. R. Cheeseman, G. Scalmani, V. Barone, G. A. Petersson, H. Nakatsuji, X. Li, M. Caricato, A. V. Marenich, J. Bloino, B. G. Janesko, R. Gomperts, B. Mennucci, H. P. Hratchian, J. V. Ortiz, A. F. Izmaylov, J. L. Sonnenberg, D. Williams-Young, F. Ding, F. Lipparini, F. Egidi, J. Goings, B. Peng, A. Petrone, T. Henderson, D. Ranasinghe, V. G. Zakrzewski, J. Gao, N. Rega, G. Zheng, W. Liang, M. Hada, M. Ehara, K. Toyota, R. Fukuda, J. Hasegawa, M. Ishida, T. Nakajima, Y. Honda, O. Kitao, H. Nakai, T. Vreven, K. Throssell, J. A. Montgomery Jr, J. E. Peralta, F. Ogliaro, M. J. Bearpark, J. J. Heyd, E. N. Brothers, K. N. Kudin, V. N. Staroverov, T. A. Keith, R. Kobayashi, J. Normand, K. Raghavachari, A. P. Rendell, J. C. Burant, S. S. Iyengar, J. Tomasi, M. Cossi, J. M. Millam, M. Klene, C. Adamo, R. Cammi, J. W. Ochterski, R. L. Martin, K. Morokuma, O. Farkas, J. B. Foresman and D. J. Fox, *Gaussian, Inc.*, Wallingford CT, 2016.
78 S. Chatterjee, M. Fellner, J. A. Rankin, M. G. Thomas, S. B. J S Rifayee, C. Z. Christov, J. Hu and R. P. Hausinger, *Biochemistry*, 2024, **63**(8), 1038–1050.
79 S. Bhunia, A. Ghatak and A. Dey, *Chem. Rev.*, 2022, **122**, 12370–12426.
80 J. C. Lewis, *Acc. Chem. Res.*, 2019, **52**, 576–584.
81 N. Lehnert, *J. Inorg. Biochem.*, 2012, **110**, 83–93.
82 M. Lundberg, P. E. M. Siegbahn and K. Morokuma, *Biochemistry*, 2008, **47**, 1031–1042.
83 A. Bassan, M. R. A. Blomberg and P. E. M. Siegbahn, *Chem.–Eur. J.*, 2003, **9**, 106–115.
84 B. L. Greene, G. E. Vansuch, C.-H. Wu, M. W. W. Adams and R. B. Dyer, *J. Am. Chem. Soc.*, 2016, **138**, 13013–13021.